

JGR Solid Earth



RESEARCH ARTICLE

10.1029/2021JB023617

Performance of a Rotational Sensor to Decipher Volcano Seismic Signals on Etna, Italy

Eva P. S. Eibl¹ , Martina Roskopf^{1,2}, Mariangela Sciotto³, Gilda Currenti³ ,
Giuseppe Di Grazia³ , Philippe Jousset⁴ , Frank Krüger¹, and Michael Weber^{1,4}

¹Institute for Geosciences, University of Potsdam, Potsdam, Germany, ²Department of Earth Sciences, Institute of Geophysics, ETH Zurich, Zurich, Switzerland, ³Istituto Nazionale di Geofisica e Vulcanologia-Osservatorio Etneo, Catania, Italy, ⁴GFZ German Research Centre for Geosciences, Potsdam, Germany

Key Points:

- We tested the performance of a rotational sensor compared to a seismometer and a seismic network using long-period (LP), volcano-tectonic (VT) events and tremor on Etna
- LP and VT events are dominated by SH- and SV-waves, respectively. Tremor changed from SH- to a mixed wavefield during strombolian eruptions
- LP event and tremor back azimuths point to the main craters consistent with the Istituto Nazionale di Geofisica e Vulcanologia location; VT event back azimuths are at times consistent

Supporting Information:

Supporting Information may be found in the online version of this article.

Correspondence to:

E. P. S. Eibl,
eva.eibl@uni-potsdam.de

Citation:

Eibl, E. P. S., Roskopf, M., Sciotto, M., Currenti, G., Di Grazia, G., Jousset, P., et al. (2022). Performance of a rotational sensor to decipher volcano seismic signals on Etna, Italy. *Journal of Geophysical Research: Solid Earth*, 127, e2021JB023617. <https://doi.org/10.1029/2021JB023617>

Received 9 NOV 2021
Accepted 22 APR 2022

Author Contributions:

Conceptualization: Philippe Jousset, Michael Weber
Formal analysis: Eva P. S. Eibl, Martina Roskopf, Mariangela Sciotto
Funding acquisition: Eva P. S. Eibl
Investigation: Eva P. S. Eibl, Martina Roskopf, Mariangela Sciotto, Gilda Currenti, Giuseppe Di Grazia, Philippe Jousset

© 2022. The Authors.

This is an open access article under the terms of the [Creative Commons Attribution License](https://creativecommons.org/licenses/by/4.0/), which permits use, distribution and reproduction in any medium, provided the original work is properly cited.

Abstract Volcano-seismic signals such as long-period events and tremor are important indicators for volcanic activity and unrest. However, their wavefield is complex and characterization and location using traditional seismological instrumentation is often difficult. In 2019 we recorded the full seismic wavefield using a newly developed 3C rotational sensor co-located with a 3C traditional seismometer on Etna, Italy. We compare the performance of the rotational sensor, the seismometer and the Istituto Nazionale di Geofisica e Vulcanologia-Osservatorio Etneo (INGV-OE) seismic network with respect to the analysis of complex volcano-seismic signals. We create event catalogs for volcano-tectonic (VT) and long-period (LP) events combining a STA/LTA algorithm and cross-correlations. The event detection based on the rotational sensor is as reliable as the seismometer-based detection. The LP events are dominated by SH-type waves. Derived SH phase velocities range from 500 to 1,000 m/s for LP events and 300–400 m/s for volcanic tremor. SH-waves compose the tremor during weak volcanic activity and SH- and SV-waves during sustained strombolian activity. We derive back azimuths using (a) horizontal rotational components and (b) vertical rotation rate and transverse acceleration. The estimated back azimuths are consistent with the INGV-OE event location for (a) VT events with an epicentral distance larger than 3 km and some closer events, (b) LP events and tremor in the main crater area. Measuring the full wavefield we can reliably analyze the back azimuths, phase velocities and wavefield composition for VT, LP events and tremor in regions that are difficult to access such as volcanoes.

Plain Language Summary Traditional seismographs usually include mass and spring systems which measure vibrations constrained to up-down, north-south and east-west directions. We compare the traditional seismometer to a rotational sensor which measures ground rotation around the same three directions. We installed a rotational sensor on Etna volcano in 2019 to test these new sensors in a volcanic environment. We compare the performance of the rotational sensor, a traditional seismometer and the Istituto Nazionale di Geofisica e Vulcanologia-Osservatorio Etneo (INGV-OE) seismometer network. We detect two types of a few second long earthquakes and find that the rotational sensor performs as good as the seismometer. We use the rotational sensor to calculate directions of the earthquake locations and find that most directions agree with the INGV-OE network location and the area of the active craters. We find that for some earthquakes the ground only moved horizontally while for others it also moved up and down. Using a rotational sensor on a volcano we can easily and reliably estimate the ground motion, the speed of the earthquake waves in the ground and understand better how these earthquakes are generated.

1. Introduction

Volcanic activity is often accompanied by a wide range of seismo-volcanic signals such as very long-period (VLP) events, long-period (LP) events, volcano-tectonic (VT) events and tremor (Chouet, 2003). These signals contain information about physical processes at depth and are used to define the activity state of a volcano (Saccorotti & Lokmer, 2021). Monitoring observatories analyze these events continuously and use the number, amplitude, location and their variation in time for early warning purposes (Wassermann, 2012).

These volcano-seismic events have distinct characteristics and underlying processes. VT earthquakes often have a broad and dominant frequency content between 2 and 20 Hz and an impulsive onset. They are similar to tectonic earthquakes in terms of failure mechanism (Saccorotti & Lokmer, 2021) and are interpreted as shear failure. LP events are defined in a narrow, low frequency band from 0.5 to 5 Hz (Chouet & Matoza, 2013) with dominant

Methodology: Eva P. S. Eibl

Project Administration: Eva P. S. Eibl

Resources: Eva P. S. Eibl, Mariangela Sciotto, Gilda Currenti, Giuseppe Di Grazia, Philippe Jousset

Supervision: Eva P. S. Eibl, Frank Krüger

Validation: Eva P. S. Eibl, Mariangela Sciotto, Giuseppe Di Grazia

Visualization: Eva P. S. Eibl, Martina Roskopf, Gilda Currenti

Writing – original draft: Eva P. S. Eibl

Writing – review & editing: Eva P. S. Eibl, Martina Roskopf, Mariangela Sciotto, Gilda Currenti, Giuseppe Di Grazia, Philippe Jousset, Frank Krüger, Michael Weber

frequency content between 0.5 and 2 Hz (Saccorotti & Lokmer, 2021). They are emergent and their source process remains debated (Saccorotti & Lokmer, 2021). VLP event waveforms are similar to LP events but are composed of frequencies in the range of 0.01–0.5 Hz (Chouet & Matoza, 2013; Cannata et al., 2009). Tremor is a long-lasting, emergent seismic signal that can show a broad spectral content or harmonic frequency content and might share similar spectral characteristics like LP events (McNutt, 2005; Saccorotti & Lokmer, 2021).

Volcano observatories use a network or array of seismic sensors to detect and locate these transient and continuous signals (Chouet & Matoza, 2013). VT events are located using P and/or S wave arrival times (Lomax et al., 2009) while LP events are located using the polarization of the wavefield (Flinn, 1965; Jurkevics, 1988), picking of the P-wave (Jousset et al., 2013), waveform similarity based function and/or amplitude decay (Cannata et al., 2013). Tremor is located using the seismic amplitude decrease or phase shifts in a network (Battaglia & Aki, 2003; Cannata et al., 2013; Di Grazia et al., 2006; Soubestre et al., 2018; Taisne et al., 2011) or within a seismic array (Bormann, 2002; Rost & Thomas, 2002).

Seismic monitoring on volcanoes is conventionally based on a network equipped with seismic translational sensors. Portable rotational sensors have also been available for a few years (Bernauer et al., 2018) enabling their use in volcano-seismology. They record the ground rotation rate around three axes. Based on one single sensor it is now possible to reliably identify and filter for specific wave types (Sollberger et al., 2020) to derive local phase velocities (Hadziioannou et al., 2012; Wassermann et al., 2016) and the back azimuth. The back azimuth is estimated based on the similarity of the rotation rates measured around the horizontal axes (Wassermann et al., 2020; Yuan et al., 2020) or the similarity of rotation rate around the vertical axis and transverse acceleration (Hadziioannou et al., 2012; Wassermann et al., 2016).

Portable rotational sensors were tested on Stromboli (Wassermann et al., 2021). They were later used during the caldera collapse in Hawaii to analyze the displacement and back azimuth of some large magnitude events (Wassermann et al., 2020). Location results were further compared with array derived rotation measurements and a navigation-type gyro on the M_w 5.4 Hualien earthquake and an earthquake swarm in central Italy (Yuan et al., 2020).

Here, we recorded volcano-seismicity at Etna volcano in August–September 2019 (Section 2) using a rotational sensor (3C) and a co-located traditional translational seismometer (3C) (in total 6C) (Section 3.1). We compare the performance of (a) the rotational sensor with respect to the co-located seismometer and (b) the 6C station with respect to the Istituto Nazionale di Geofisica e Vulcanologia-Osservatorio Etno (INGV-OE) seismic network. We use STA/LTA algorithms and cross-correlation to detect events (Section 3.2), estimate signal-to-noise-ratios (Section 3.3) and source back azimuths using two different methods (Section 3.4). We create LP and VT event catalogs (Section 4.1), describe the detected VT events (Section 4.2), LP events (Section 4.3) and tremor (Section 4.4). We discuss the quality of the event catalog of the rotational sensor in comparison to the seismometer catalog (Section 5.1). We compare our estimated back azimuths for VT events, LP events and tremor with the locations from the INGV-OE and discuss systematic offsets and other discrepancies (Section 5.2, 5.3 and 5.4). We finally discuss phase velocities for SH-type waves in the LP events and tremor (Section 5.5), the wavefield separation (Section 5.6), possible tilt contamination (Section 5.7) and highlight the good performance of the rotational sensor and additional wavefield information we can extract.

2. Volcanological Framework

Etna volcano is located in eastern Sicily north of Catania, Italy (Figure 1). It is an active basaltic stratovolcano in a complex geodynamic environment controlling the volcanic activity (Patane et al., 2000). It is characterized by frequent eruptive episodes, consisting of lava effusion and explosive phenomena spanning from strong strombolian and lava fountain activity (Currenti & Bonaccorso, 2019) to very powerful eruptive episodes producing tall plumes (e.g., Andronico et al., 2021; Cappello et al., 2019; Corsaro et al., 2017). Less frequent, but posing high risks, are eruptions occurring at fractures opening on the flanks of Etna due to dyke intrusion (e.g., Cannavo et al., 2019; Currenti et al., 2011). In addition, during non-eruptive periods, the summit craters degas constantly (Zuccarello et al., 2013).

In 2019 Etna showed explosive activity of variable intensity and weak ash emissions from all the summit craters. After the explosive activity taking place in July at the South East and North East craters, and throughout the first

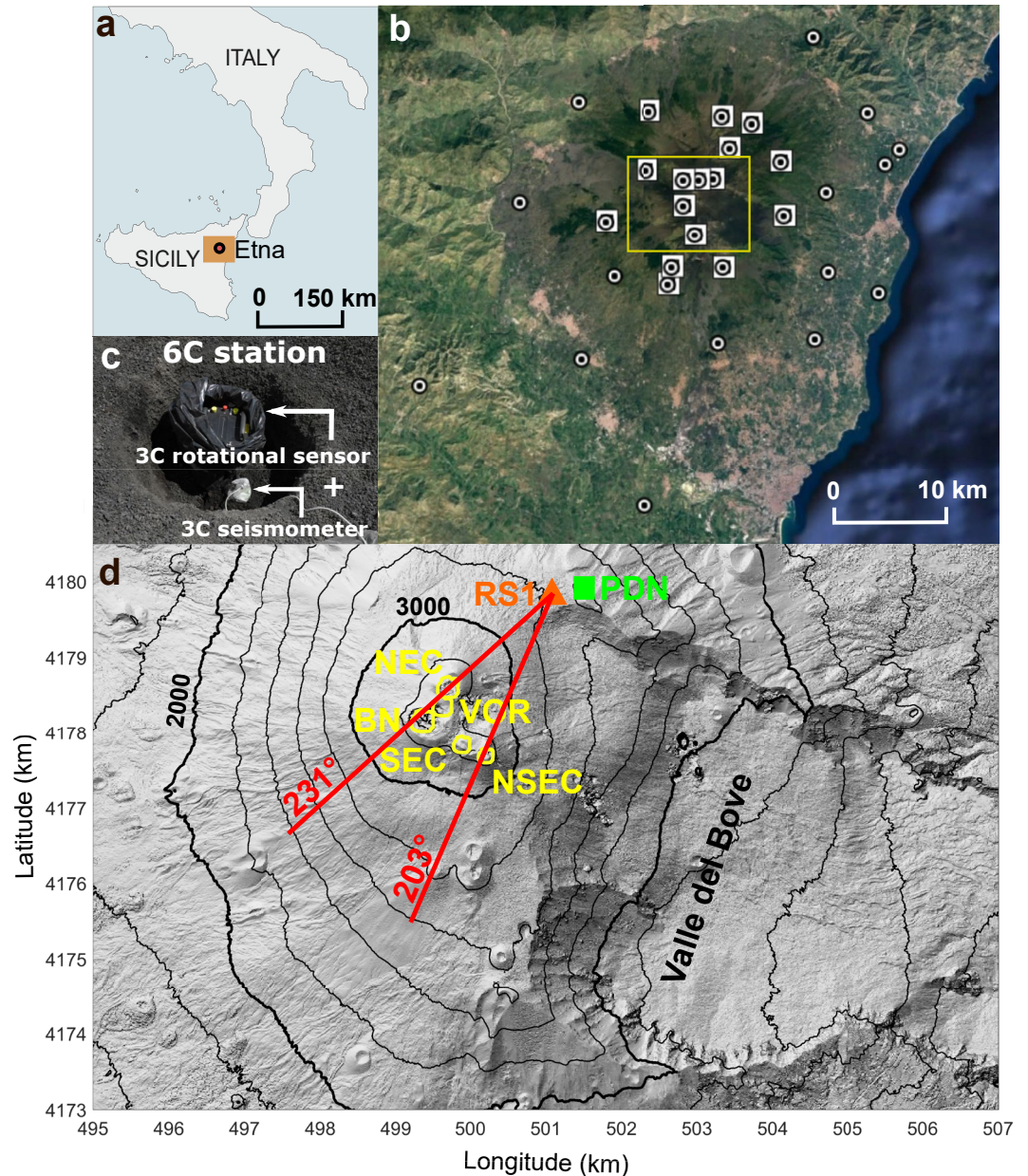


Figure 1. Overview of instrument installation on Etna volcano, Italy. (a) Location of Etna in Italy. (b) Istituto Nazionale di Geofisica e Vulcanologia-Osservatorio Etneo seismic network including stations used for VT event location (white circles with black dot) and for LP event and tremor location (white squares). (c) Installing the 3C seismometer (light with cable) and the 3C rotational sensor (black) on the same granitic base plate constitutes our 6C instrument at RS1. (d) Installation site RS1 (orange) near the Pizzi Deneri Observatory (green, PDN). We use the denomination for the summit craters at the time of the observations: North East (NEC), Voragine (VOR), Bocca Nuova (BN), South East (SEC) and New South East (NSEC) (yellow). Latitude and longitude are given in the UTM33S system. DEM with height in m (Palaseanu-Lovejoy et al., 2020).

half of the field deployment, volcanic activity mainly consisted of ordinary degassing and weak ash emissions. On 6 September sustained strombolian activity resumed at North East and Voragine craters. While at this latter crater it exhausted in a couple of days, at the North East crater it intensified producing sustained strombolian explosions from 8 to 11 September. The following day, activity again resumed at Voragine crater (Giuffrida et al., 2021). Volcanic activity at this crater consisted of strombolian explosions, which led to the growth of a small scoria cone inside the crateric area, and lasted for the whole period of measurements. In addition, lava overflows within the Voragine crater area took place from 18 to 21 September.

3. Data Acquisition and Data Analysis

3.1. Instrument Setup and Preprocessing

We co-located a 3C blueSeis-3A rotational sensor (iXblue) and a 3C Trillium Compact 120 s seismometer (Nanometrics) to form a 6C station (Figure S1 in Supporting Information S1). We installed it from 24 August to 23 September 2019 at RS1 in the ZR network (Eibl et al., 2022) on the northern flank of Etna near the Pizzi Deneri Observatory. This is at about 2 km distance from the summit craters in a flat area that consists surficially of unconsolidated pyroclastic material (Branca et al., 2011; Napoli et al., 2021). The two sensors were installed on the same $35 \times 35 \times 3$ cm³ granitic base plate at about 40 cm depth enclosed by backfilled pyroclastic material to avoid wind noise. The instruments recorded at 200 Hz sampling rate and were linked to a communication cube (CCUBE) and data cube (DATA-CUBE3), respectively, for data storage. The setup was powered using three solar panels of 140 W each and three batteries of 75 Ah each (Figure 1). We oriented the rotational sensor and seismometer using a Quadrans fiber-optical gyro compass. The Quadrans is not affected by magnetic minerals in the ground and our sensor is hence properly aligned to geographic north.

The blueSeis-3A is a three component fiber-optic gyroscope measuring the rotational wavefield. It is a portable, broadband, low noise sensor with high dynamic range. It has no moving parts, a flat response over a wide frequency range (DC to about kHz) and is not sensitive to translational motion. The measurement principle is based on the Sagnac effect. For more information the reader is referred to Figure S1 in Supporting Information S1, Bernauer et al. (2018) and Izgi et al. (2021).

The rotational sensor data output is proportional to rad/s and we deramp, demean and detrend it. We demean, detrend, taper and instrument correct (based on a poles and zeros deconvolution) the seismometer data to true ground velocity for event detection and to acceleration for the back azimuth estimate. We trim both datasets to the time window of interest and apply an acausal, zero-phase Butterworth bandpass filter of order 4 before further processing (see Section 3.2). We exclude data on 12 September between 10:20 and 11:30 and 14 September between 10:17 and 11:20 due to field work near the instruments.

3.2. Event Detection Using a STA/LTA Algorithm and Cross-Correlation

We create a seismic event catalog applying a STA/LTA algorithm to the seismometer data. We create a separate event catalog using a cross-correlation method on the seismometer data. We consider only events included in both catalogs in the final event catalog of the seismometer. We repeat the same steps on rotational sensor data to create a final event catalog for the rotational sensor. Before creating the catalogs we bandpass filter the waveforms between 10 and 20 Hz for VT events and between 0.2 and 1 Hz for LP events. We hence analyze a smaller part of possible LP (0.5–1 Hz) and VLP (0.2–0.5) events here, to detect them more reliable in the seismometer and rotational sensor data (Figures 3 and 5). We refer to these events as LP events throughout the text.

For the first catalog we apply a short-time over long-time average (STA/LTA) algorithm (Trnkoczy, 2012) as implemented in the Snuffler analysis software (Heimann et al., 2017) to detect events. Before applying the STA/LTA algorithm we test various window lengths and choose for LP events a STA window of 12 s and an LTA window of 48 s. The STA and LTA windows for VT events are set to 10 and 50 s, respectively. The thresholds used for the VT and LP event catalog are 2 and 2.8, respectively.

For the second catalog we use the cross-correlation function of ObsPy (Beyreuther et al., 2010) to cross-correlate predefined templates of VT and LP events with the whole data set. We choose twelve 10 s long VT events with varying source locations and magnitudes based on the INGV-OE earthquake catalog (Alparone et al., 2020, Section 3.5). For LP events we randomly choose four 12 s long events over time. For these events we calculate the cross-correlation for the seismometer using templates from the seismometer and for the rotation sensor using templates from the rotational sensor. To detect VT and LP events the cross-correlation value had to exceed 0.3 and 0.8, respectively. We check both the final catalog based on rotational data and the final catalog based on seismometer data manually to remove false triggers.

We test various thresholds for the STA/LTA algorithm and cross-correlation. We choose the above mentioned thresholds since they yield the highest overlap with events listed in the INGV-OE catalog but do not yield an excessive amount of false picks.

3.3. Signal to Noise Ratio Calculation

We calculate the signal-to-noise ratio (SNR) in two non overlapping time windows: one containing the noise before the event and one containing the event. We test time windows between 1 and 10 s and here show results for a 4 s long time window for VT events and a 6 s long time window for LP events. We calculate the root mean square (RMS) in these windows and calculate the SNR for each component:

$$SNR_j = \frac{\sqrt{\frac{1}{n} \sum_{i=0}^n S_{ji}^2}}{\sqrt{\frac{1}{n} \sum_{i=0}^n N_{ji}^2}} \quad (1)$$

where n is the number of samples in the time window, S the amplitude of the signal and N the amplitude of the noise. The index j refers to the east, north or z component. We apply Equation 1 to calculate the SNR for each component and each sensor separately. To compare the sensors further we use the component with the largest SNR when comparing SNR values of LP events.

For VT events we calculate an averaged SNR as the sum of the squared signal of all three components before applying the square root:

$$SNR = \frac{\sqrt{\frac{1}{n} \sum_{i=0}^n S_{ei}^2 + S_{ni}^2 + S_{zi}^2}}{\sqrt{\frac{1}{n} \sum_{i=0}^n N_{ei}^2 + N_{ni}^2 + N_{zi}^2}} \quad (2)$$

where indexes e , n , and z refer to the east, north and vertical component, respectively. To calculate the SNR we filter the waveforms between 2 and 5 Hz for VT events and 0.6–1.4 Hz for LP events.

3.4. Back Azimuth Estimate Using Rotational Motion

S-waves polarized in the vertical plane (SV) and Rayleigh waves are only recorded on the horizontal rotational components. The measured ground motion on these components can be used to derive the back azimuth of the wave (Langston & Liang, 2008). To do this Wassermann et al. (2020) perform an orthogonal distance regression on the horizontal rotational motion components $\dot{\Omega}_E$ and $\dot{\Omega}_N$. This approach has a 180° ambiguity unless seismometer data are available. The correlation of the corresponding radial acceleration and transverse rotation rate is in phase for the correct quadrant.

We use a 1.5 s long window with 90% overlap for VT events filtered from 2 to 5 Hz and a 30 min long window for tremor filtered from 0.5 to 2.5 Hz. The settings for the tremor are identical to the settings used by INGV-OE to allow comparison.

S-waves polarized in the horizontal plane (SH) and Love waves are only recorded on the vertical rotational component. We use the vertical rotation rate $\dot{\Omega}_z$ and transverse acceleration a_t to directly calculate the back azimuth and the phase velocity. For SH-type waves the vertical rotation rate and transverse acceleration waveforms are similar except for a factor of $-0.5 \cdot c$ where c is the phase velocity (Sollberger et al., 2018).

In a moving time window we first loop over all possible back azimuths with a step size of 1° (Hadziioannou et al., 2012). We calculate for each back azimuth the transverse acceleration using the north and east acceleration. In a second loop we cross-correlate this with the vertical rotation rate. The correct back azimuth yields the largest cross-correlation value. In time windows where the correlation value exceeds 0.75 we calculate the phase velocity.

To resolve the back azimuth of local LP events filtered between 0.6 and 1.4 Hz we use a 5 s long time window with 90% overlap. We use a 30 min long window without overlap for tremor filtered from 0.5 to 2.5 Hz in accordance with the INGV-OE processing.

We test window lengths from 1.5 s to 30 min depending on the event type. Based on the short event duration of LP and VT events, we finally choose short windows to extract the single phase arrivals and minimize scattering. For

tremor we choose a longer window that is consistent with the processing used for the INGV-OE tremor locations. If the source migrates within this time window it affects our back azimuth estimate.

3.5. INGV-OE Event Location Based on a Seismic Network

To validate the results obtained, and to highlight detection and characterization capability of the rotational sensor, we compare our event catalogs with the catalogs of the INGV-OE. The permanent seismic network run by INGV-OE consists of about 30 broadband (40 s cutoff period), three-component Trillium 40 s seismometers (Nanometrics). Of the whole network, 16 stations are used to retrieve volcanic tremor centroid, and to detect and localize low frequency events (Figure 1b). They acquire data in real time at a sampling rate of 100 Hz.

VT events reported here belong to the “Mt. Etna Revised and Concise Seismic Catalog from 1999 (EtnaRCSC) (INGV)” (Alparone et al., 2020). The catalog contains the main hypocenter parameters of Etna’s earthquakes revised by the “Gruppo Analisi Dati Sismici” of INGV-OE. When triggering for VT events, data are often unfiltered and classified VT events have a frequency content above 5.5 Hz.

The INGV-OE constrains the centroid location of the volcanic tremor source with a temporal resolution of 30 min by applying a grid search method based on the seismic amplitude decay with distance (for details see Di Grazia et al. [2006] and Cannata et al. [2013]). First the seismic signal is filtered from 0.5 to 2.5 Hz, where most of volcanic tremor energy is concentrated at Mt. Etna. An R^2 value (goodness of fit) is computed (Cannata et al., 2013; Di Grazia et al., 2006). Volcanic tremor locations, which are automatically carried out at INGV-OE, are revised and a minimum number of stations and a minimum value of goodness of fit are set to extract reliable solutions.

At INGV-OE two real-time automatic systems are implemented to detect LP and VLP events in the frequency band 0.5–5.5 Hz and 0.05–0.5 Hz, respectively. This detection is based on a STA/LTA trigger algorithm (Trnkoczy, 2012). Source locations of these events are retrieved, similarly to the volcanic tremor location algorithm, by means of a grid search method implementing computation of a function: For LP source location the method uses the sum of the semblance function (Neidell & Taner, 1971) and R^2 value, and for VLP events the radial semblance (Cannata et al., 2013). We compare our LP catalogs to a subset of detected events by INGV-OE that have a peak frequency in the 0.2–1 Hz range. For the back azimuth comparison we further constrain the INGV-OE catalog. Our constraints are located events with a corresponding event in the rotational catalog, a radial semblance goodness value of more than 0.6, a semblance plus R^2 goodness value of more than 1.55 and locations in the summit area (497.6–501.6 km longitude and 4176.3–4180.3 km latitude).

4. Results

4.1. Event Catalogs Using Seismometer Only and Rotational Sensor Only in Comparison to the INGV-OE Catalog

4.1.1. VT Event Catalog

We create two catalogs based on rotational sensor and seismometer data to detect VT events and compare this to the INGV-OE VT event catalog. Using rotational sensor data the STA/LTA algorithm detects 2059 VT events while the cross-correlation detects 259 VT events. The final VT event catalog includes a total of 140 events for the rotational sensor (Figure 2a).

Using the seismometer the STA/LTA algorithm detects 2734 VT events. The cross-correlation detects 321 events and in the final VT event catalog we list 147 VT events for the seismometer (Figure 2a).

We detect VT events in the whole time period except for 7–9 September 2019. In general, the number of events per day in the catalog follows the same trend for both sensor types (Figure 2a).

The INGV-OE catalog lists 294 VT earthquakes from 24 August to 23 September 2019. 56% and 65% of the events in the final rotational and final seismometer catalogs are listed in the INGV-OE catalog, respectively. We detect the majority of events on both sensors since 107 events are comprised in both final catalogs. There is no clear temporal pattern in the event number (Figure 2c). 33 and 40 VT events are only listed in the rotational and seismometer catalog, respectively.

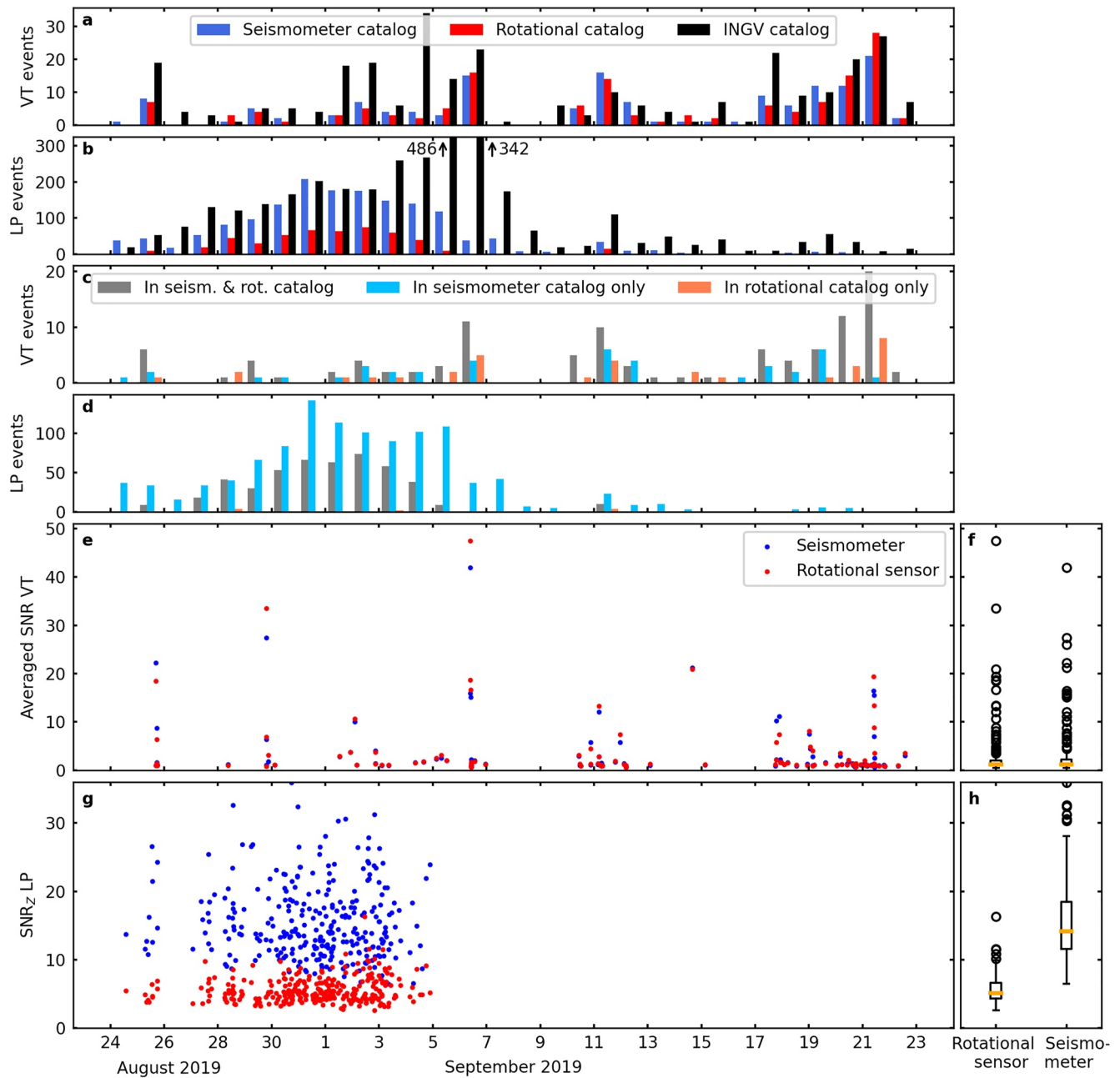


Figure 2. Daily number of detected long-period (LP) and volcano-tectonic (VT) events using the seismometer, rotational sensor and the Istituto Nazionale di Geofisica e Vulcanologia-Osservatorio Etneo (INGV-OE) network. (a and b) Number of (a) VT and (b) LP events in the final catalog based on seismometer data (blue), rotational sensor data (red) and the INGV-OE catalog (black). (c and d) Number of (c) VT and (d) LP events in both final catalogs (rotational sensor and seismometer) (gray), the rotational catalog only (orange) and the seismometer catalog only (lightblue). (e) The averaged signal-to-noise ratios (SNR) of three components for all VT events recorded by the blueSeis-3A sensor (blue) and seismometer (red) bandpass filtered between 2 and 5 Hz. (f) Boxplots summarizing the SNR distribution in panel (e). The box represents the upper and lower quartiles while the orange line marks the median of the data. The whiskers mark the variability while circles mark outliers. (g and h) Same as panels (e and f) for LP events filtered 0.6–1.4 Hz. Note that the SNR is given for the vertical component only.

4.1.2. LP Event Catalog

Based on only the vertical component of the rotational sensor, the STA/LTA algorithm detects 1404 LP events, while the cross-correlation detects 1252 LP events. The final catalog contains 488 LP events (Figure 2b).

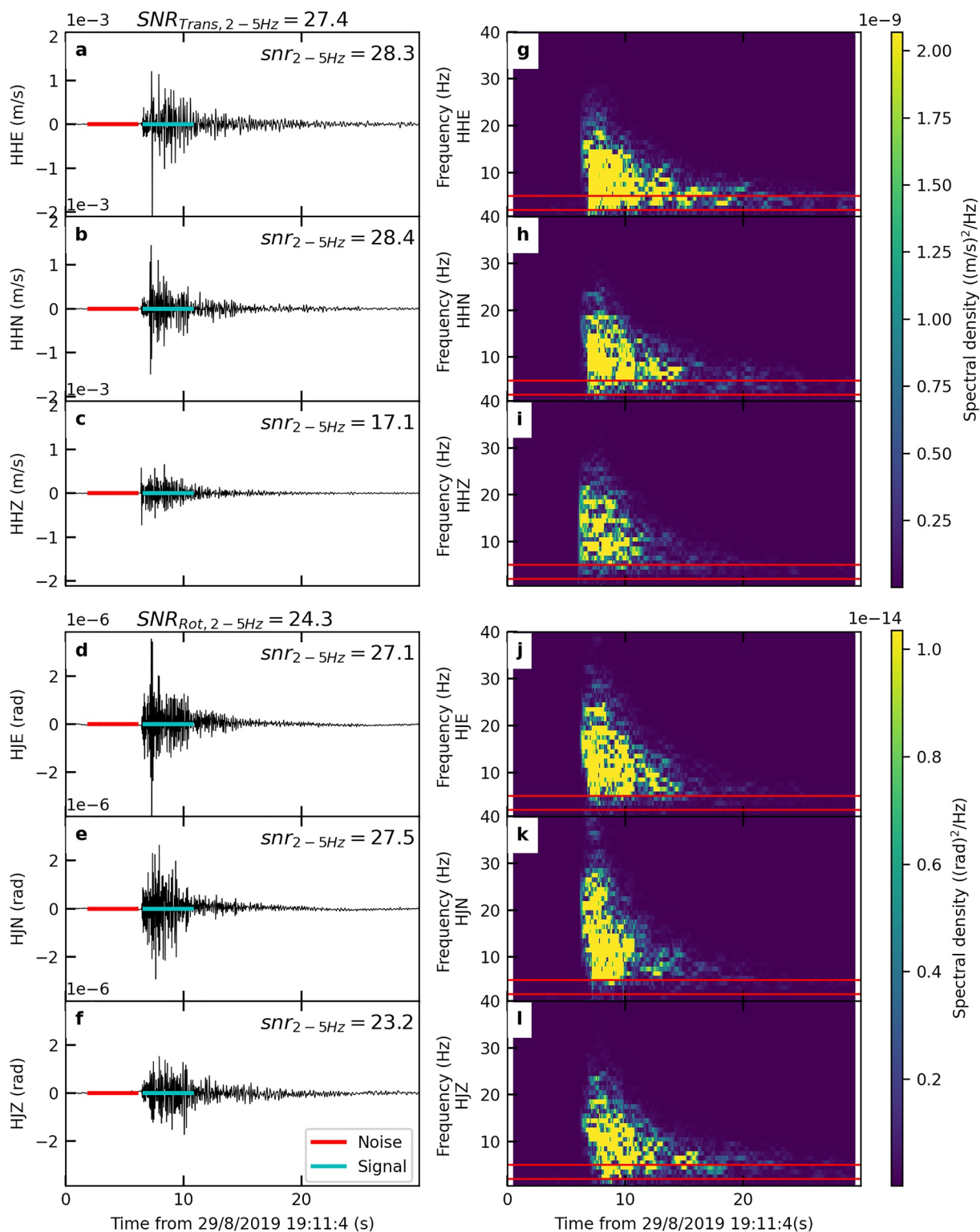


Figure 3. (a–f) Seismograms and (g–l) spectrograms of a MI 1.9 volcano-tectonic event close to the main craters at 19:11 on 29 August. Panels (a–c and g–i) show the seismometer data and (d–f and j–l) the rotational sensor data for the E , N , and Z component. Note the different amplitude and color scale to aid visual comparison of the events recorded by different sensor types, especially for the spectral density. In panels (a–f) the horizontal lines mark a 4 s window duration for the noise (red) and signal (cyan) in the signal-to-noise ratio (SNR) ratio calculation. The mean SNR (Equation 2) can be found on top of the seismograms while we display the SNR for each component (Equation 1) in the right upper corner of each seismogram. In panels (g–l) the red lines mark the frequency band of the SNR calculation.

To compile the LP event catalog based on the seismometer data, we use all three translational components. The STA/LTA algorithm detects 3395 events while the cross-correlation detects 2341 events. The final catalog contains 1595 events (Figure 2b).

The total number of LP events in the two final catalogs is three times larger for the seismometer. Most LP events in the rotational catalog are also listed in the seismometer catalog (Figure 2d). The number of events per day follow the same trend in time: most LP events occur between 27 August and 4 September (Figure 2b). The INGV-OE catalog lists 3358 LP events from 24 August to 23 September 2019 (Figure 2b). 24% and 27% of the events in the final rotational and final seismometer catalog are listed in the INGV-OE catalog, respectively. 474 LP events are listed in both the final rotational and final seismometer catalog (Figure 2d). 14 LP events and 1121 LP events are only listed in the rotational and seismometer catalog, respectively. 97% of the events detected by the rotational sensor are also detected by the seismometer. The detections of the rotational sensor are hence reliable.

4.2. Volcano-Tectonic Earthquakes

4.2.1. VT Event Characteristics and Signal to Noise Ratios

We investigate the spectral properties of the VT event wavefield in our catalog from 0.6 to 40 Hz. One VT event occurred for example, on 29 August at 19:11 close to the summit craters at 1.7 km distance from the station (Figure 3).

The event duration is less than 20 s and most energy is between 1 and 25 Hz (Figure 3). The maximum amplitude of the integrated horizontal rotational components is around 2.5×10^{-6} rad and for the vertical around 1×10^{-6} rad, whereas the translational components show maximum amplitudes of 1×10^{-3} m/s on the horizontal and 5×10^{-4} m/s for the vertical component.

For 60% of the VT events the SNR is higher on the rotational sensor in comparison to the seismometer. The SNR ratios range from 1 to 20 with 2% outliers up to 50 for both instrument types (Figures 2e and 2f). The temporal pattern of SNRs for both instruments are similar. The distance between upper and lower quartiles in the boxplot (Figures 2e and 2f) is slightly larger for the rotational sensor.

4.2.2. VT Event Back Azimuth Estimate Using the Horizontal Rotation Rates

For VT events the amplitude and SNR on the horizontal rotational components is higher than on the vertical rotational component. We hence estimate the back azimuth using the horizontal components (Wassermann et al., 2020) of all VT events filtered from 2 to 5 Hz and compare it to the back azimuth estimated from the INGV-OE catalog location. We categorize the events into four subclasses depending solely on the stability and consistency of the two back azimuth results at the arrival time of the P wave and the following 3 s. The frequency content is not considered when classifying the VT events.

For Subclass 1 events the back azimuths are consistent with the back azimuth derived from the INGV-OE location and the difference of all points in this time window is less than 20° . We detect the P wave of an event on 25 August at 17:27 (Figure S2 in Supporting Information S1) around second 14 of the time window. The calculated back azimuth at the signal onset is in good agreement with the back azimuth estimated from the INGV-OE catalog location. Some events yield the correct back azimuth at the time of the signal onset for only 1–2 s.

For Subclass 2 events the estimated values increase several tens of degrees at the P wave onset time around the back azimuth derived from the INGV-OE catalog. Subclass 3 events have a stable offset of $70\text{--}130^\circ$ between the calculated and the INGV-OE back azimuth. For Subclass 4 events we detect no energy in the frequency band between 2 and 5 Hz. These VT events also had signal-to-noise ratios below 3 (Figure 4b) and MI magnitudes below 1.5.

We also assess the spatial distribution of the defined event groups (Figure 4a). For VT events with epicentral distance above 3 km and event depth of 4–6 km, the estimated back azimuths are in agreement with the values derived from the INGV-OE catalog, whereas for events within a distance of 3 km the values are not always consistent (Figure 4a).

Based on our VT event catalog we estimate the minimum magnitude needed at each distance to record sufficient energy for a back azimuth calculation (Figure 4b). We do not detect large distance events of small magnitude and

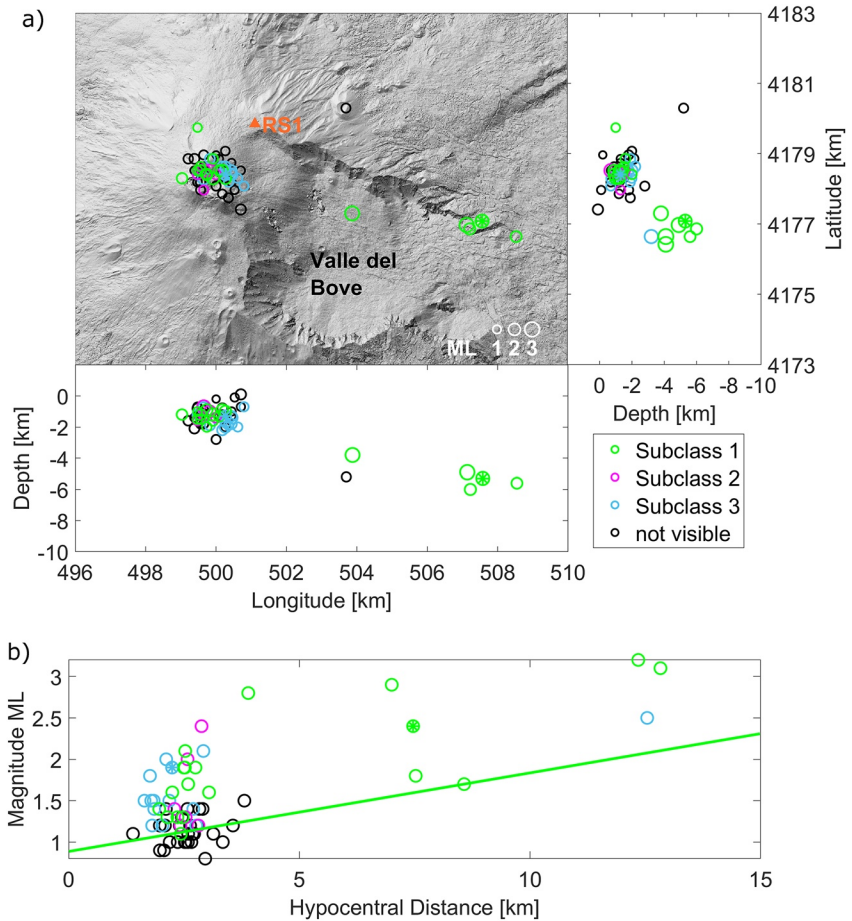


Figure 4. Volcano-tectonic (VT) event locations according to the Istituto Nazionale di Geofisica e Vulcanologia-Osservatorio Etno (INGV-OE) catalog colored according to the quality of our back azimuth estimate. (a) VT events with back azimuth consistent (Subclass 1), unstable (Subclass 2), stable but offset (Subclass 3) and not visible in comparison to the INGV-OE catalog location. The orange triangle indicates the instrument location RS1. (b) Magnitude versus hypocentral distance for VT events color-coded by their back azimuth results. The green line indicates the minimum event magnitude of events where we resolve the correct back azimuth with respect to distance. Stars represent the VT events on 25 August (Subclass 1, green; Figure S2 in Supporting Information S1) and 29 August (Subclass 3, lightblue; Figure 3).

do not estimate the back azimuth. For distances around 2 km, some events with magnitudes above the green line did not yield reliable back azimuths due to low energy in the frequency band from 2 to 5 Hz.

4.3. Long-Period Events

4.3.1. LP Event Characteristics and Signal to Noise Ratios

We present the full wavefield recording of an LP event on 2 September at 11:11:19 (Figure 5). We detect the LP event on all components of the seismometer. The seismic ground velocities are largest on the east component. The vertical ground velocity is three to four times smaller than the ground velocity measured on the horizontal components. In Figure 5 most energy is around 1 Hz and visible on all three components. The LP event is in most cases only detected on the integrated vertical component of the rotational sensor hence indicating a dominant SH-type wave motion. The dominant frequency is similar to the seismometer recording. Some LP events are visible on the integrated north component but at a four times smaller amplitude than the integrated vertical component (Figure 5).

The SNR_z for LP events ranges from 8 to 30 for the seismometer and 3–16 for the rotational sensor (Figures 2g and 2h). The SNR is hence larger on the seismometer but more scattered.

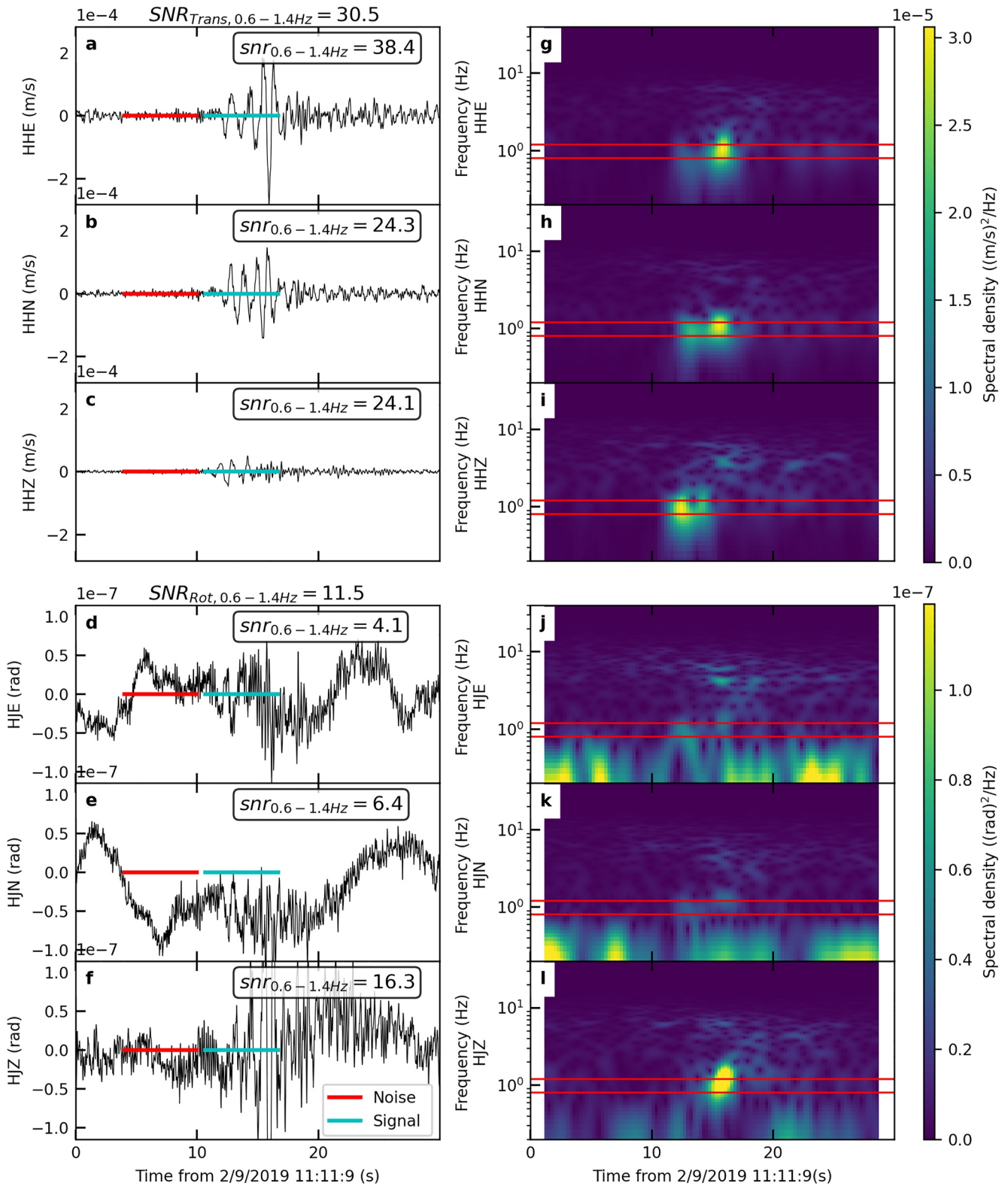


Figure 5. Seismograms and spectrograms of a long-period event at 11:11:19 on 2 September that has the highest signal-to-noise ratio. Subfigures as in Figure 3.

4.3.2. LP Event Back Azimuth Estimate Using Vertical Rotation Rate and Transverse Acceleration

We estimate the back azimuth of the LP events using the vertical rotation rate and the transverse acceleration (Hadziioannou et al., 2012) due to the dominant SH-wave content (Figure 6). The back azimuth estimate is reliable due to high correlation coefficients and small uncertainties. For the LP event on 2 September at 11:11:19 the cross-correlation coefficient increases during the LP event (Figure 6). The estimated back azimuth is around 200° (Figure 6b) while the phase velocities increase to 1,000 m/s (Figure 6c).

We extracted the dominant back azimuths of all LP events (Figure 6d). In time windows that show large cross-correlation coefficients the dominant back azimuth is stable between 160 and 220° for 8 s which coincides with the direction toward the New South East and Voragine craters and an area further south. This is in broad agreement with the INGV-OE locations for LP events (Figure 6e).

4.4. Volcanic Tremor Characteristics and Back Azimuth Estimate

Volcanic tremor persisted throughout our experiment (Figure 7). The volcanic tremor amplitude underwent a first slight and rapid increase, which lasted for a few hours in the night from 7 to 8 September. It increased further in the morning of 9 September and remained high until the morning of 13 September 2019, except for a brief time interval in the night between 11 and 12 September.

The volcanic tremor source in August and early September contained energy up to 3 Hz with most energy around 1 Hz (Figures S3 and S4 in Supporting Information S1). This tremor source amplitude is largest on the vertical rotational component and the east component of the seismometer. It is weaker but visible on the north component of the seismometer. It is not visible on the horizontal rotational components and the vertical component of the seismometer. Hence the persistent tremor wavefield is dominated by SH-type waves. The SH-type component of the tremor source is stable around 190–200° and points toward the southern summit area (Figure 7e). Due to the low energy in the SV-wavefield, we do not show the corresponding not reliable tremor back azimuths (Figure 7f).

From 8 to 13 September the tremor intensified and the frequency content is broad with energy from 0.5 to more than 10 Hz on all components of both sensors (Figures S3 and S4 in Supporting Information S1). In this time period volcanic tremor probably consists of the sum of several sources and the wavefield is composed of both SV- and SH-type wave motion while the SH-type wavefield is stronger. On 8 September the SV-type waves migrate to 280° and on 9 September to 240° (Figure 7f). The SH-type wavefield of the tremor source migrates to 200–220° on 9 to 13 September (Figure 7e). In this time period the tremor wavefield is composed of SV- and SH-type waves and originates in the crater area based on the back azimuths.

5. Interpretation and Discussion

5.1. Quality of the Event Catalogs

The absolute number of VT events in the final catalogs and the daily event number is similar for the rotational sensor and seismometer. The rotational sensor can hence detect VT events similar to the seismometer. This also holds for LP events, although we only detect energy on the vertical component of the rotational sensor but all three translational components. Therefore, we detect LP events easily on the seismometer when considering all three components for event detection since the SNR is larger (Figure 5). Due to the lower 3-component SNR for the rotational sensor, we detect only a third of the LP events using the vertical component of the rotational sensor in comparison to the 3-components of the seismometer. The higher self-noise of the rotational sensor in comparison to the seismometer (Bernauer et al., 2018) might hinder the LP event detection on the horizontal components. We detect LP events reliably due to high thresholds in the STA/LTA algorithm and cross-correlations.

30%–97% of the LP events and 73%–76% of VT events are listed in both catalogs (Figures 2c and 2d). Hence, some VT and LP events only trigger on one sensor and are partly not visible on the other sensor (e.g., LP events on the horizontal rotational components). This highlights the different sensitivity of the sensor with respect to events which might cause more rotation or more translation. In addition, waveform types within an event might differ. While the vertical rotational component is sensitive to SH-type waves, a shift to SV-type waves leads to larger amplitudes on the horizontal rotational components (Wassermann et al., 2020). In addition, a heterogeneous ground might affect the sensitivity of the sensor inducing for example, additional rotation (Yuan et al., 2020).

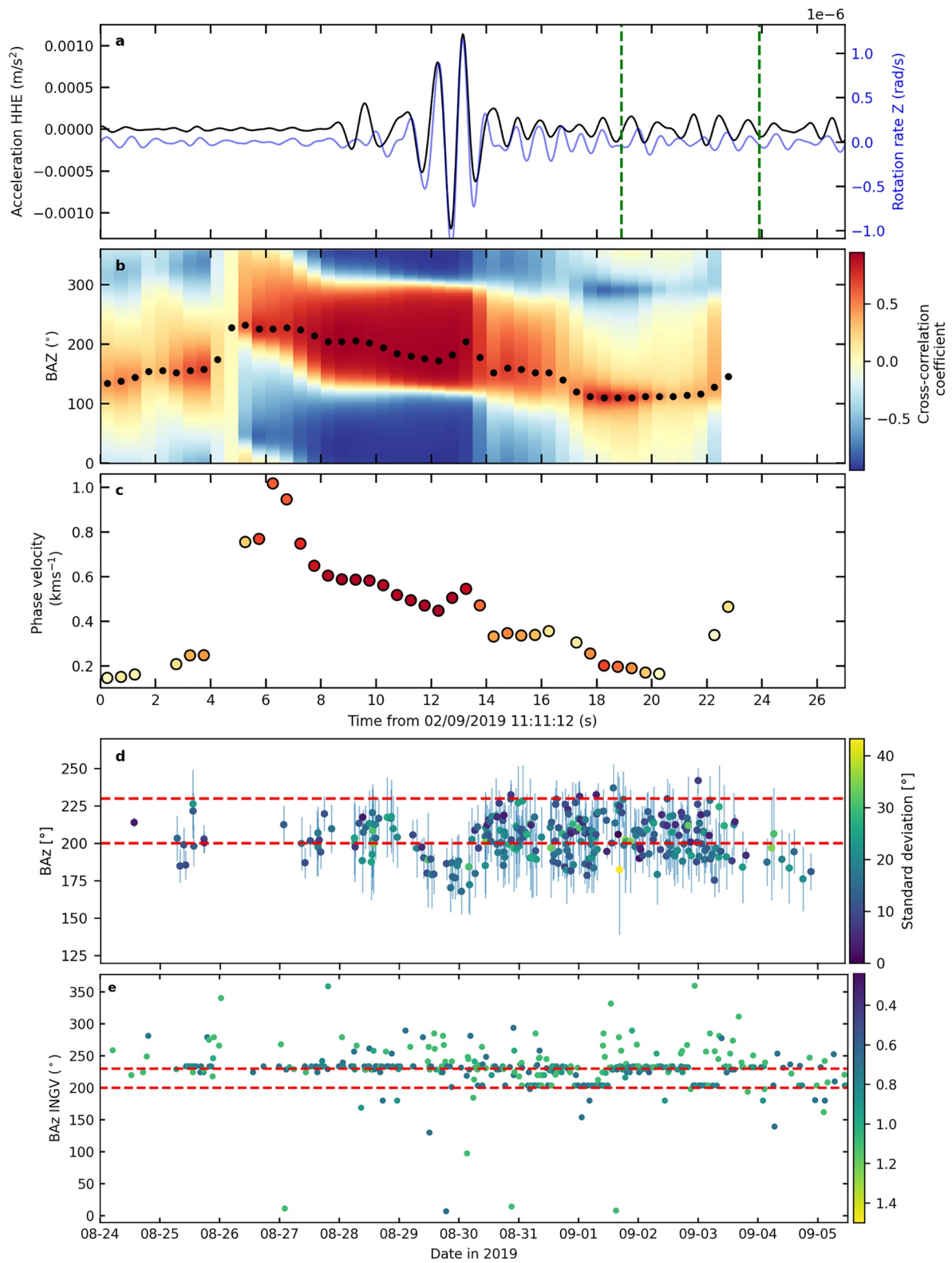


Figure 6.

27% and 32% of VT events identified by INGV-OE are listed in our final rotational and seismometer catalog, respectively (Figure 2a). The INGV-OE uses a seismic network around Etna for their event detection, whereas here only one station was used. We do not detect events with small magnitudes from the INGV-OE catalog, events at large distance or a combination of both. Attenuation and scattering in the heterogeneous volcanic edifice along the travel path to the station affect the events (Giampiccolo et al., 2007; Patane et al., 1994; Zieger et al., 2016). We only list events detected by both the STA/LTA algorithm and the cross-correlation approach in our final catalog. This hence reduces the number of false triggers but also the number of events (Section 4.2). While far events might be picked up by cross-correlations values, the amplitude might be damped so that the STA/LTA algorithm does not detect it.

We compare our detections with LP event detections by INGV-OE with peak frequencies in the same frequency band. 4% and 13% of LP events in the INGV-OE catalog are listed in our final rotational and seismometer catalog, respectively (Figure 2b). The discrepancy between our and INGV-OE catalogs is most likely caused by the different detections in a network in comparison to a single station. During 3 to 6 September the INGV-OE detected a lot more events than our instruments. This might be due to the very low amplitudes of LP events on those days. The decrease in LP event number from 7 to 10 September (Figure 2b) is due to the increase of the volcanic tremor amplitude and hence the low signal-to-noise-ratios (Figure 7). De Barros et al. (2011) and Cannata et al. (2009) reported a similar anti-correlation of the LP event number and tremor amplitude in 2008 on Etna. Nevertheless, INGV-OE and our occurrence rate show the same pattern until the increase of volcanic tremor which accompanied the intensification of explosive activity.

In addition, we detect VT events in this study that are not listed in the INGV-OE catalog. These events have large cross-correlations coefficients with events close to the main craters and hence occurred within 2 km distance of our station. A visual inspection of these events allows to verify that most of them are scarcely energetic ($M < 1.3$), recorded only at few stations, and hence their hypocenters are poorly constrained. Until 2019, INGV-OE earthquake catalog did not include this type of events.

Given the similar absolute number of events the single rotational sensor performs as good as the seismometer for VT events while the seismometer performs better for the LP events due to the waveform properties. A combination of both sensors or network of sensors likely outperforms our single station approach with respect to event catalog completeness.

5.2. Event Location and Generation of VT Events in Comparison to the INGV-OE Catalog

We compare the back azimuth of earthquakes in the INGV-OE catalog and the back azimuth derived from the rotational sensor and seismometer. Events from the southeast and at far distance are well located, while 25% of the events in the summit area are not well located. The deviating back azimuth estimate from the back azimuth derived using the INGV-OE catalog for Subclass 2 and 3 events cannot be explained by lower magnitudes, lower SNR or different frequency content compared to Subclass 1 events.

Discrepancies between VT event locations from the INGV-OE catalog and back azimuth estimates based on our rotational sensor might be caused by properties of the ground, the topography, the short epicentral distance, the source or scattered wave paths as suggested by Yuan et al. (2020). Scattering in the wavefield of VT events might result from small-scale structures, which have stronger impact on high frequencies (Yuan et al., 2020) and are likely to be present at a volcano. Zuccarello et al. (2016) for example, reported that the mechanical properties of the uppermost few hundred meters of rock in volcanic environments such as Mount Etna vary strongly. The sensors were installed in a plane area near Pizzi Deneri filled with unconsolidated pyroclastic material. This heterogeneous subsurface might lead to scattering (Giampiccolo et al., 2007) and attenuation (Giampiccolo et al., 2007; Zieger et al., 2016). The spatial scattering might be visible in the clustering of the Subclass 3 events.

Figure 6. Back azimuth estimates for one long-period (LP) event (a–c) and the whole catalog (d–e). (a) We bandpass filter the waveforms of the vertical rotation rate component (blue) and the acceleration on the east component (black) of the LP event on 2 September at 11:11:19 between 0.6 and 1.4 Hz. The vertical, green lines indicate the moving time window of 5 s used with 90% overlap. (b) Black points highlight the back azimuth with the highest cross-correlation coefficient while colors indicate the cross-correlation coefficients. (c) Phase velocities are color-coded using the highest correlation coefficients of vertical rotation rate and transverse acceleration. (d) For each LP event in both catalogs we extract all back azimuth values with a correlation threshold above 0.9 (see panel [b]). In subfigure d we display the mean (points) and standard deviation (color and vertical lines) of these back azimuth values for each event. Horizontal red lines indicate the range of back azimuths of the craters. (e) Back azimuth of event locations in the Istituto Nazionale di Geofisica e Vulcanologia-Osservatorio Etneo catalog for the events in subfigure (d). Note the different azimuth ranges in panels (d and e).

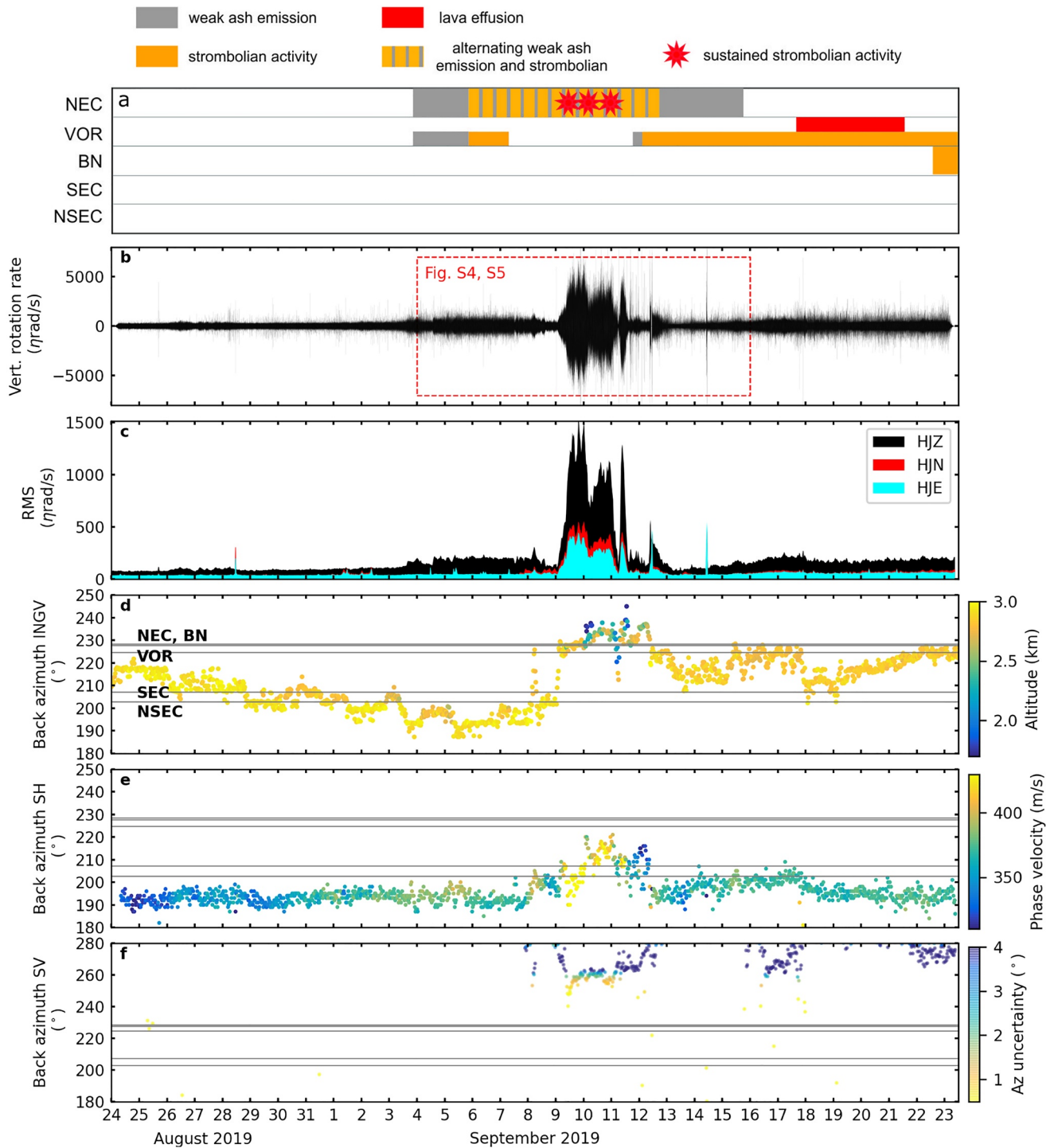


Figure 7. Tremor source back azimuth estimate. (a) Activity of the summit craters. (b) Background tremor and tremor increase visible on the vertical component of the rotational sensor. (c) Root mean square of the tremor amplitude filtered from 0.5 to 2.5 Hz using a 30 min long window without overlap on all three rotation rate components, (d) Back azimuth estimated from tremor locations based on amplitude location method using the Istituto Nazionale di Geofisica e Vulcanologia-Osservatorio Etneo network colored according to altitude. We indicate the back azimuths (gray lines) of the craters (see Figure 1). (e and f) Back azimuth of tremor with no overlap and a window length of 900 s using the (e) vertical rotation rate and transverse acceleration (Hadziioannou et al., 2012) colored according to estimated SH-wave phase velocity and (f) horizontal rotational components (Wassermann et al., 2020) colored according to azimuth uncertainty. Note that the back azimuth estimate is only reliable from 8 September when the energy on the horizontal components increased.

Additionally, the topography in Figure 4a indicates a scarp south of the station toward Valle del Bove (Figure 1). This and other not directly visible complex structures around the main craters might add to the scattering of VT events in this region.

A systematic offset between the actual source and seismic array back azimuth (here referred to as squinting) can be caused by topography or waveguides (Eibl et al., 2017; Krueger & Weber, 1992; Schweitzer, 2001). Similar to seismic arrays our rotational sensor might be affected by squinting. Our VT event study highlights a spread between INGV-OE location and our back azimuths. However, since no systematic difference between our back azimuths and the event locations in a similar area seems to be present we conclude that the VT event location is not affected by squinting.

For the VT events most energy is at frequencies below 10 Hz but energy is visible up to 25 Hz (Figure 3). Milana et al. (2008) reported similar dominant frequencies below 10 Hz for seismometer data.

In the frequency band from 2 to 5 Hz 60% of the VT events had larger SNR ratios for the rotational sensor. Yuan et al. (2020) do not confirm the larger SNR of rotation rates, but the authors concluded, that the SNR of a blueSeis-3A is almost as large as for a Trillium Compact seismometer (for a frequency band between 0.1 and 20 Hz). A study by Bernauer et al. (2021) obtained SNRs for the blueSeis-3A around 200 calculating the RMS in a 1 s window for a close and explosive source. The SNR for a strong VT event is in a similar range. Due to the larger SNR in the frequency band between 10 and 20 Hz we use this setting for event detection to improve the picking accuracy (Figures 3g–3l).

We could not list any events in our final VT event catalog from 7 to 9 September. This might correlate with the high volcanic tremor amplitude on 7 and 8 September and its further increase from 9 to 13 September. However, events detected while the tremor amplitude is large (7–13 September) do not have smaller SNR compared to events at times with low tremor activity. Additionally, we detect VT events after 9 September, when the tremor amplitude is still large (Figure 7b). Discrepancies in back azimuth estimates based on the horizontal rotational components or the vertical rotational component are also reported by Wassermann et al. (2020). These components act as wave type filters and are only sensitive to SV-type waves or SH-type waves, respectively. These different wave types might be scattered differently by structures in the subsurface or might be generated at different locations. Wassermann et al. (2020) found a 35° difference in back azimuth and attribute it to scattering/reflection of SV-type waves at a steep and prominent fault scarp, scattering or to anisotropy.

VT events can be located using the S-P travel time difference on a single station. However, several 6C stations are necessary for LP event and tremor location and hence a systematic comparison is not made here.

5.3. Event Location and Generation of LP Events in Comparison to the INGV-OE Catalog

LP events typically have dominant frequencies in the range of 0.5–2 Hz (Chouet & Matoza, 2013). Based on a narrow filter used for LP event picking, we here report a dominant frequency around 1 Hz which is consistent with the observations of the INGV-OE in the same time period. This is also consistent with the frequency content of LP events in the past. Falsaperla et al. (2002) reported LP events on Etna for the first time and found peak frequencies at 3, 3.3, and 3.5 Hz. In the following years Cannata et al. (2009) observed the frequency peak with the largest amplitude in the range of 0.4 to more than 10 Hz and most energy in a frequency range from 0.4 to 0.8 Hz. Similarly, Saccorotti et al. (2007) reported dominant LP event frequencies of 0.6 and 3 Hz while tremor had a peak frequency of 1 Hz and De Barros et al. (2009) observed a dominant frequency of LP events between 0.3 and 1.2 Hz.

We find that the SH-type waves compose the LP events on Etna. Cannata et al. (2009) performed a network-based polarization analysis of LP events detected from November 2003 to May 2006. Assuming a source location near the crater they conclude that the wave motion at stations 5–8 km from the summit filtered from 0.4 to 0.8 Hz is consistent with Rayleigh or SV waves. At the close stations they noted with respect to the craters a temporal change in dominant waves from transverse wave motion, to P waves (radial wave motion). They speculate that this change could be caused by a source migration or change in source excitation. While for example, LP events close to the surface might be dominated by Love waves a deeper source might be dominated by P waves (Aki & Richards, 2002; Cannata et al., 2009). Similarly, Lokmer et al. (2008) observed on Etna that the polarization changed from transverse to radial around the end of an eruption in 2005.

Based on the discussion of Cannata et al. (2009) this might imply a shallow LP event source or special excitation or orientation of a crack in our 2019 data set. Lokmer et al. (2008) suggested that a transverse crack resonance is possible depending on the lithostatic pressure and the local stress field where LP events are tightly linked to the way a crack discharges fluids. Falsaperla et al. (2002) reported that the LP event is dominated by both body and surface waves while being dominated by SH waves. Saccorotti et al. (2007) conclude that the onset of the LP event recordings is at most stations dominated by radial wave motion while the largest amplitude indicated shear wave motion. This might indicate a radiation from a non-isotropic source or a topography effect since the pattern is similar at several (but not all) stations in a network. Here, we do not record a transition in wave type but a pure SH-type wave motion.

After 4 September, in coincidence with a gradual and slight increase of volcanic tremor amplitude, the number of LP events shows a significant drop. Due to their narrow, dominant frequencies (around 1 Hz) tremor might hide LP events especially when using a STA/LTA algorithm. However, at the time the tremor decreased, the LP events with dominant frequencies around 1 Hz did not reappear. Similarly, Lokmer et al. (2008) reported a change in LP event waveforms, increase in intensity, dominant frequency and Q factor during and after an eruption.

The back azimuth estimate of LP events are more consistent than for VT events. The more narrow and lower frequency band for LP events leads to longer wavelengths and hence less influence of spatial heterogeneities (Bean et al., 2008). However, studies by Cesca et al. (2008) and Bean et al. (2008) also showed that low velocity layers have a significant impact on the signal. The authors state that LP events usually occur at less than 800 m depth and most likely in or close to the low velocity layer, shortening the wavelength of LP events making them more sensitive to heterogeneous structures. In the past, LP events usually occurred at 0–2,000 m depth below the summit craters of Etna (Falsaperla et al., 2002; Lokmer et al., 2007; Patane et al., 2008; Saccorotti et al., 2007). De Barros et al. (2011) located LP events at 20–700 m depth while Lokmer et al. (2008) located them at 400–1,600 m below the summit craters. Sources of most of the LP events of the INGV-OE catalog in this time period locate at less than 2 km depth and a few degrees further north (Figure 6e). For sources around the craters the expected back azimuths are in the range of 200–230° (Figure 1) which is consistent with the LP event back azimuths derived here (Figure 6d). Saccorotti et al. (2007) located events at less than 800 m depth and suggested a crack-like geometry causing the non-isotropic radiation and shear wave motion.

Comparing the LP event and tremor locations with permanent seismic network based locations from INGV-OE, our event locations are systematically 10–20° further south than the active crater on 13 September or the crater directions. The back azimuths derived using the SH-type wavefield of LP events and tremor might hence be affected by squinting. If the LP event is located in the southern sector of the plumbing system the waves have to cross the shallow plumbing system of the Voragine and New South East crater on the way to the station and might additionally be affected by topography and local structure such as faults that distort some frequencies. Using 3D finite difference modelling, Jousset et al. (2022) showed that the velocity distribution in the volcano is a major contributor to explain the wavefield distortion at Piano delle Concazze, and might therefore explain the back azimuth discrepancy for some events.

5.4. Event Location and Generation of Volcanic Tremor in Comparison to the INGV-OE Location

Volcanic tremor is always present at Etna and its energy is mostly concentrated in the frequency band of 0.5–2.5 Hz (Cannata et al., 2013). In August and early September we obtain back azimuths of 190–200° (Figure 7e) for the SH-type waves. Due to the low energy in the 0.5–2.5 Hz band on the horizontal rotational components (SV-type waves) (Figure S3 in Supporting Information S1), we discard the SV wave back azimuths. The wavefield is dominated by SH-type waves for which our back azimuth based on the vertical rotation rate and transverse acceleration is consistent with the INGV-OE locations (Figure 7d).

Volcanic tremor intensified during the activity from 9 September 2019. In this time period both SH- and SV-type waves compose the wavefield (Figure 7c) while the tremor source moved to larger depths according to the INGV-OE location (Figure 7d). The back azimuth estimated using the vertical rotational component migrated to a location closer to the active crater on 8 September and the shift toward Voragine/North East crater on 10 September is in accordance with the activity change. From 9 September the North East crater was more active and from 12 September the activity moved to Voragine crater. This is consistent with the observed increase in

tremor amplitude. From our station location the latter craters are both aligned, which hence prevents a distinction among them.

The INGV-OE located the source of volcanic tremor from 7 to 8 September below the summit craters, and from 9 to 12 September below the Voragine crater and the North East crater. From 9 to 15 September it is at the beginning located below the North East crater and by the end of the week below the Voragine crater. From 10 to 12 September the tremor source is located at 1.6 km altitude while it is close to 3 km altitude most of the time. Therefore, while the tremor source migrates closer to the site of the rotational sensor it also migrates to larger depth. We see a slight increase in phase velocity from 300 to 400 m/s at the same time. The slight discrepancy in back azimuth in early September might be caused by the radiation pattern on Etna that might affect the amplitude-based locations in the 0.5–2.5 Hz band. Similarly, Saccorotti et al. (2004) reported a discrepancy in observed and expected tremor back azimuth of two arrays and suggested that the topography and/or the medium heterogeneity affected the wave propagation.

5.5. Phase Velocity Estimate

We estimate phase velocities for SH-type waves using the vertical rotation rate and the transverse acceleration. The phase velocity is a direct byproduct of the back azimuth estimate and yields more insight into the local medium properties. It is worth investigating and quantifying this further in the future.

In general, we derive SH-wave phase velocities for LP events that range from 500 to 1,000 m/s (Figure 6c) while the tremor phase velocities range from 300 to 400 m/s (Figure 7e). Saccorotti et al. (2004) reported values of 1,000 m/s on Etna. Bean et al. (2014) mentioned P-wave velocities of 1.8 km/s in the top 800 m, which results in Rayleigh wave velocities of 855 m/s. Zuccarello et al. (2016) found shear velocities below 400–450 m/s for depths down to 60 m and around 600–700 m/s at depths between 60 and 130 m for a halfspace and a v_p/v_s ratio of 2. The velocities resolved by Zuccarello et al. (2016) are lower than the ones by Bean et al. (2014) and consistent with the here estimated seismic wave velocities for LP events.

Currenti et al. (2021) measured the strain rate along the axial direction of a 1.5 km long fiber optic cable at high temporal and spatial resolution using distributed acoustic sensing measurements (DAS). They performed several comparisons between DAS and broadband signals during the 2018 and 2019 experiments and estimated the apparent seismic phase velocity at Pizzi Deneri. Thanks to the fiber coverage and high resolution they noted a high variability of the seismic phase velocity due to the presence of local features, for example, faults. On average the obtained values range from 300 to 1,000 m/s with lower values in correspondence with a fault zone. They estimated the apparent phase velocity also for an LP event recorded on 27 August 2019, when the rotational sensor was recording. Currenti et al. (2021) obtained a value of about 1,000 m/s for a good match between DAS strain and seismic velocity under the plane wave assumption. Their estimate is in agreement with the phase velocity computed from rotational and translational components at RS1 (Figure 6c), which is not crossed by local faults. Further consistent phase velocities ranging from 200 to 700 m/s at 0 to 100 m below the scoria layer, were derived from jumps close to the DAS cable using multichannel analysis of surface waves (Jousset et al., 2022). This comparison is beneficial since the consistent and independent results show that the method is reliable. In addition, it shows that—at our site at 2 km from the craters—the plane wave assumption is fulfilled for relating strain and rotation with seismic velocity measurements.

5.6. Wavefield Separation

The rotational sensor is a unique instrument that allows us to separate waves in a wavefield such as SH and SV-waves. We can hence easily note that LP events are dominated by SH-type waves before the event is located. Similarly, we note a dominant SH-wave component in the volcanic tremor that changed to a mixture of SH- and SV-type when sustained strombolian activity started. These wavefield characteristics are beneficial when it comes to detecting subtle changes in the wavefield or new tremor sources. This is an advantage in comparison to the use of a single translational seismometer.

This wavefield information can help to better constrain the source mechanism of volcano-seismic events. Based on seismometer data, the source mechanism of LP-events and tremor was in the past least constrained. For example, the source mechanism of LP events on Etna was discussed once the event was located and the wavefield

properties defined (Aki & Richards, 2002; Cannata et al., 2009; Lokmer et al., 2008; Saccorotti et al., 2007). However, in some cases the wavefield properties could only be discussed once a location was assumed since the ground motion pattern was inconsistent on the stations in the network (Cannata et al., 2009). The rotational sensor simplifies the procedure since the wavetype is directly and clearly accessible. We hence think that the rotational sensor is more beneficial with respect to LP events and tremor.

The seismometer can detect the P-wave that is in a homogeneous medium not associated with any rotational motion and hence not detected by the rotational sensor. While a weak S-wave might be clearly picked up by the rotational sensor, both the P- and S-wave arrival time can be used to estimate the distance of the event. Adding a rotational sensor to a seismometer network is hence beneficial for the research.

5.7. Tilt Contamination of Seismometer Data

Rotational sensors are not sensitive to translational ground motion and purely record the ground rotation. In contrast, seismometers are sensitive to rotational ground motion that add to the true translational motion and hence affects the amplitude of the recorded signal (Rodgers, 1968).

Examples of tilt contamination were reported on the horizontal components of an ocean-bottom seismometer from 5 to 13 s period (Lindner et al., 2017), broadband seismic recordings at less than 50 s period in the near-field of explosions at Stromboli (Wielandt & Forbriger, 1999), and VLP recordings at Asama Volcano in Japan (Maeda et al., 2011), Mt. Merapi (10–30 s period) (Van Driel et al., 2015) and during the 2018 caldera collapse at Kilauea (Flinders et al., 2020).

Attempts to correct for this tilt contamination include forward modeling of tilt observed on co-located tiltmeters (Flinders et al., 2020) or rotational sensors (Lindner et al., 2017) and an inversion method using Green's functions that account for the seismometer response to synthetic tilt motion (Maeda et al., 2011; Van Driel et al., 2015). In addition, the tilt can be estimated using the differences in vertical and horizontal displacements measured by different instruments installed at the same site (Wielandt & Forbriger, 1999). The rotational sensor can help to detect such seismometer tilting and helps to correct it before being misinterpreted as translational ground motion.

LP events, VT events and tremor recordings presented in this study are not affected by tilt. To assess this, we estimate the tilt on the horizontal seismometer components using the largest recorded VT earthquake in our catalog (ML 3.2). It occurred on 4 September 2019 at 15:52:29. The seismometer recorded a maximum horizontal acceleration (square root of the sum of the squared translation on the horizontal axes) of $1.0 \times 10^{-2} \text{ m/s}^2$. To estimate the order of possible tilt contamination, we integrate the rotation rate data to rotation and demean it. We calculate the square root of the sum of the squared rotation on the horizontal axes and derive a tilt angle of $3.2 \times 10^{-7} \text{ rad}$. We multiply the maximum tilt angle with a gravitational acceleration of 9.81 m/s^2 according to formula 2.2. in Wielandt and Forbriger (1999) and derive an additional horizontal acceleration due to tilt of $3.2 \times 10^{-6} \text{ m/s}^2$ for unfiltered seismic data. This is 1/3248 of the measured maximum acceleration. We repeat the procedure with data filtered into different frequency bands and find a tilt contribution of 1/1825 between 0.5 and 2.5 Hz (tremor band), 1/1529 between 0.6 and 1.4 Hz (LP event band) and 1/14 between 0.01 and 0.5 Hz (VLP event band). So while other studies have demonstrated tilt contamination in seismic records of VLP events, the tilt contribution is negligible for the LP events, VT events, and tremor analyzed here.

6. Conclusion

We detect and analyze VT events, LP events and volcanic tremor in a 30 day long data set of a rotational sensor and a seismometer on Etna volcano, Italy. Defining VT and LP event catalogs using either rotational sensor or seismometer data lead to a similar event detection rate for both sensors.

The spectral content of VT events recorded on the rotational sensor is similar to the seismometer recordings. In a frequency range of 2–5 Hz the signal-to-noise-ratios of the rotational sensor are similar to the seismometer. 56%–65% of our VT event detections are listed in the INGV-OE catalog based on a seismic network.

We mainly detect LP events on the vertical component of the rotational sensor and they hence consist of SH-type waves. This results in lower thresholds for the LP event detection for the rotational sensor compared to the seismometer, where we detect events on all three components. Despite this difference, the LP event detection is

reliable and 97% of the events detected by the rotational sensor are also detected by the seismometer. Hence, LP events can be detected using a single rotational sensor.

Depending on the wavefield characteristics of the detected events we apply a suitable method for back azimuth estimate based on rotational sensor data. VT events generate more rotation on the horizontal rotational components which we hence use for the back azimuth estimate. We resolve correct event back azimuths for 31% of the VT events close to the main craters. The heterogeneity of Etna's subsurface might affect this. Additionally, events within 3 km distance should have at least magnitudes around MI 1–1.2 and a SNR above 3 to be detected. For LP events we use a cross-correlation of transverse acceleration and vertical rotation rate to calculate the back azimuth. Our results indicate that LP events originate in the direction of the main craters, which is consistent with past LP event locations on Etna and locations from INGV-OE.

Finally, we use the rotational sensor to separate the waves in the tremor wavefield. We record a SH-wave tremor wavefield during time of weak activity changing to a SH- and SV-wave dominated wavefield during sustained strombolian activity. The back azimuth is consistent with the amplitude-based location from INGV-OE and the changes in phase velocity match in time with the tremor source depth changes.

The back azimuth codes by Wassermann et al. (2020) and Hadziioannou et al. (2012) show great potential to be applied to VT events, LP events and tremor on volcanoes. They are originally written for seismic signals with different dominant frequencies and signal duration. Event detection can be performed in a similar manner as using the seismometer. Back azimuth, wave types and phase velocities can now be extracted using merely two co-located instruments, that is, a 3C rotational and a 3C seismometer, respectively. The analysis and interpretation of the rotational data can enhance our understanding in a remote or dangerous volcanic environment.

Conflict of Interest

The authors declare no conflicts of interest relevant to this study.

Data Availability Statement

Seismic data of this experiment is available through GEOFON (<https://doi.org/10.14470/ME7564062119>). We used freely available software from the Pyrocko (Heimann et al., 2017) and Obspy toolboxes (Beyreuther et al., 2010).

Acknowledgments

We thank the “Parco dell’Etna” and the municipalities (Linguaglossa and Castiglione di Sicilia) for the permit to deploy the instruments in the Etna national park. We thank Daniel Vollmer (University of Potsdam) and Danilo Contrafatto, Graziano Larocca, Daniele Pellegrino and Mario Pulvirenti (INGV-OE Sezione di Catania) for support with logistics and in the field. This work was financially supported by Eurovolc (Grant No. 731070) and the Daimler Benz Foundation (32-02/18). Open access funding enabled and organized by Projekt DEAL.

References

- Aki, K., & Richards, P. G. (2002). *Quantitative seismology* (2nd ed.) University Science Books.
- Alparone, S. C., Barberi, G., Di Grazia, G., Ferrari, F., Giampiccolo, E., Maiolino, V., et al. (2020). *Mt. Etna revised and concise seismic catalog from 1999 (EtnARCSC)*. Istituto Nazionale di Geofisica e Vulcanologia (INGV). <https://doi.org/10.13127/ETNASC/ETNARCSC>
- Andronico, D., Cannata, A., Di Grazia, G., & Ferrari, F. (2021). The 1986–2021 paroxysmal episodes at the summit craters of Mt. Etna: Insights into volcano dynamics and hazard. *Earth-Science Reviews*, 220, 103686. <https://doi.org/10.1016/j.earscirev.2021.103686>
- Battaglia, J., & Aki, K. (2003). Location of seismic events and eruptive fissures on the Piton de la Fournaise volcano using seismic amplitudes. *Journal of Geophysical Research*, 108(B8), 2364. <https://doi.org/10.1029/2002JB002193>
- Bean, C. J., Lokmer, I., & O'Brien, G. (2008). Influence of near-surface volcanic structure on long-period seismic signals and on moment tensor inversions: Simulated examples from Mount Etna. *Journal of Geophysical Research*, 113(8). <https://doi.org/10.1029/2007JB005468>
- Bean, C. J., De Barros, L., Lokmer, I., Métaixian, J. P., O'Brien, G., & Murphy, S. (2014). Long-period seismicity in the shallow volcanic edifice formed from slow-rupture earthquakes. *Nature Geoscience*, 7(1), 71–75. <https://doi.org/10.1038/ngeo2027>
- Bernauer, F., Behnen, K., Wassermann, J., Egdorf, S., Igel, H., Donner, S., et al. (2021). Rotation, strain, and translation sensors performance tests with active seismic sources. *Sensors*, 21(1), 1–23. <https://doi.org/10.3390/s21010264>
- Bernauer, F., Wassermann, J., Guattari, F., Bigueur, A., Gaillot, A., Toldi, E. D., et al. (2018). BlueSeis3A: Full characterization of a 3C broadband rotational seismometer. *Seismological Research Letters*, 89(2A), 620–629. <https://doi.org/10.1785/0220170143>
- Beyreuther, M., Barsch, R., Krischer, L., Megies, T., Behr, Y., & Wassermann, J. (2010). ObsPy: A Python toolbox for seismology. *Seismological Research Letters*, 81(3), 530–533. <https://doi.org/10.1785/gssrl.81.3.530>
- Bormann, P. (2002). Seismic signals and noise. In P. Bormann (Ed.), *New manual of seismological observatory practice 2 (NMSOP-2)* (Vol. 1, pp. 1–34). Deutsches GeoForschungsZentrum GFZ. <https://doi.org/10.2312/GFZ.NMSOP-2>
- Branca, S., Coltelli, M., Groppelli, G., & Lentini, F. (2011). Geological map of Etna volcano, 1:50,000 scale. *Italian Journal of Geosciences*, 130(3), 265–291. <https://doi.org/10.3301/IJG.2011.15>
- Cannata, A., Di Grazia, G., Aliotta, M., Cassisi, C., Montalto, P., & Patanè, D. (2013). Monitoring seismo-volcanic and infrasonic signals at volcanoes: Mt. Etna case study. *Pure and Applied Geophysics*, 170(11), 1751–1771. <https://doi.org/10.1007/s00024-012-0634-x>
- Cannata, A., Hellweg, M., Di Grazia, G., Ford, S., Alparone, S., Gresta, S., et al. (2009). Long period and very long period events at Mt. Etna volcano: Characteristics, variability and causality, and implications for their sources. *Journal of Volcanology and Geothermal Research*, 187(3–4), 227–249. <https://doi.org/10.1016/j.jvolgeores.2009.09.007>

- Cannavo, F., Sciotto, M., Cannata, A., & Di Grazia, G. (2019). An integrated geophysical approach to track magma intrusion: The 2018 Christmas Eve eruption at Mount Etna. *Geophysical Research Letters*, *46*(14), 8009–8017. <https://doi.org/10.1029/2019GL083120>
- Cappello, A., Ganci, G., Bilotta, G., Corradino, C., Hérault, A., & Del Negro, C. (2019). Changing eruptive styles at the south-east crater of Mount Etna: Implications for assessing lava flow hazards. *Frontiers in Earth Science*, *7*, 1–10. <https://doi.org/10.3389/feart.2019.00213>
- Cesca, S., Battaglia, J., Dahm, T., Tessmer, E., Heimann, S., & Okubo, P. (2008). Effects of topography and crustal heterogeneities on the source estimation of LP event at Kilauea volcano. *Geophysical Journal International*, *172*(3), 1219–1236. <https://doi.org/10.1111/j.1365-246X.2007.03695.x>
- Chouet, B., & Yamamoto, M. (2003). Volcano seismology. *Pure and Applied Geophysics*, *160*, 739–788. <https://doi.org/10.1016/B978-044452748-6.00073-0>
- Chouet, B. A., & Matoza, R. S. (2013). A multi-decadal view of seismic methods for detecting precursors of magma movement and eruption. *Journal of Volcanology and Geothermal Research*, *252*, 108–175. <https://doi.org/10.1016/j.jvolgeores.2012.11.013>
- Corsaro, R. A., Andronico, D., Behncke, B., Branca, S., Caltabiano, T., Ciancitto, F., et al. (2017). Monitoring the December 2015 summit eruptions of Mt. Etna (Italy): Implications on eruptive dynamics. *Journal of Volcanology and Geothermal Research*, *341*, 53–69. <https://doi.org/10.1016/j.jvolgeores.2017.04.018>
- Currenti, G., & Bonaccorso, A. (2019). Cyclic magma recharge pulses detected by high-precision strainmeter data: The case of 2017 inter-eruptive activity at Etna volcano. *Scientific Reports*, *9*(1), 1–7. <https://doi.org/10.1038/s41598-019-44066-w>
- Currenti, G., Jousset, P., Napoli, R., Krawczyk, C., & Weber, M. (2021). On the comparison of strain measurements from fibre optics with a dense seismometer array at Etna volcano (Italy). *Solid Earth*, *12*(4), 993–1003. <https://doi.org/10.5194/se-12-993-2021>
- Currenti, G., Napoli, R., & Del Negro, C. (2011). Toward a realistic deformation model of the 2008 magmatic intrusion at Etna from combined DInSAR and GPS observations. *Earth and Planetary Science Letters*, *312*(1), 22–27. <https://doi.org/10.1016/j.epsl.2011.09.058>
- De Barros, L., Bean, C. J., Lokmer, I., Saccorotti, G., Zuccarello, L., O'Brien, G. S., et al. (2009). Source geometry from exceptionally high resolution long period event observations at Mt Etna during the 2008 eruption. *Geophysical Research Letters*, *36*(24), 1–5. <https://doi.org/10.1029/2009GL041273>
- De Barros, L., Lokmer, I., Bean, C. J., O'Brien, G. S., Saccorotti, G., Métaixian, J. P., et al. (2011). Source mechanism of long-period events recorded by a high-density seismic network during the 2008 eruption on Mount Etna. *Journal of Geophysical Research*, *116*(1), 1–17. <https://doi.org/10.1029/2010JB007629>
- Di Grazia, G., Falsaperla, S., & Langer, H. (2006). Volcanic tremor location during the 2004 Mount Etna lava effusion. *Geophysical Research Letters*, *33*(4), 1–4. <https://doi.org/10.1029/2005GL025177>
- Eibl, E. P., Bean, C. J., Jónsdóttir, I., Höskuldsson, A., Thordarson, T., Coppola, D., et al. (2017). Multiple coincident eruptive seismic tremor sources during the 2014–2015 eruption at Holuhraun, Iceland. *Journal of Geophysical Research: Solid Earth*, *122*(4), 2972–2987. <https://doi.org/10.1002/2016JB013892>
- Eibl, E. P. S., Vollmer, D., Jousset, P., Currenti, G., Contrafatto, D., Larocca, G., et al. (2022). 1-month seismological experiment on Etna, Italy in 2019. GFZ Data Services. Other/Seismic Network. <https://doi.org/10.14470/ME7564062119>
- Falsaperla, S., Privitera, E., Chouet, B., & Dawson, P. (2002). Analysis of long-period events recorded at Mount Etna (Italy) in 1992, and their relationship to eruptive activity. *Journal of Volcanology and Geothermal Research*, *114*(3–4), 419–440. [https://doi.org/10.1016/S0377-0273\(01\)00299-2](https://doi.org/10.1016/S0377-0273(01)00299-2)
- Flinders, A. F., Johanson, I. A., Dawson, P. B., Anderson, K. R., Haney, M. M., & Shiro, B. R. (2020). Very-long-period (VLP) seismic artifacts during the 2018 caldera collapse at Kilauea, Hawaii. *Seismological Research Letters*, *91*(6), 3417–3432. <https://doi.org/10.1785/0220200083>
- Flinn, E. A. (1965). Signal analysis using rectilinearity and direction of particle motion. *Proceedings of the IEEE*, *53*(12), 1874–1876. <https://doi.org/10.1109/PROC.1965.4462>
- Giampiccolo, E., D'Amico, S., Patanè, D., & Gresta, S. (2007). Attenuation and source parameters of shallow microearthquakes at Mt. Etna Volcano, Italy. *Bulletin of the Seismological Society of America*, *97*(1B), 184–197. <https://doi.org/10.1785/0120050252>
- Giuffrida, M., Scandura, M., Costa, G., Zuccarello, F., Sciotto, M., Cannata, A., & Viccaro, M. (2021). Tracking the summit activity of Mt. Etna volcano between July 2019 and January 2020 by integrating petrological and geophysical data. *Journal of Volcanology and Geothermal Research*, *418*, 107350. <https://doi.org/10.1016/j.jvolgeores.2021.107350>
- Hadziioannou, C., Gaebler, P., Schreiber, U., Wassermann, J., & Igel, H. (2012). Examining ambient noise using colocated measurements of rotational and translational motion. *Journal of Seismology*, *16*(4), 787–796. <https://doi.org/10.1007/s10950-012-9288-5>
- Heimann, S., Kriegerowski, M., Isken, M., Cesca, S., Daout, S., Grigoli, F., et al. (2017). *Pyrocko - An open-source seismology toolbox and library*. V. 0.3 (Technical Report). GFZ. <https://doi.org/10.5880/GFZ.2.1.2017.001>
- Izgi, G., Eibl, E. P. S., Donner, S., & Bernauer, F. (2021). Performance test of the rotational sensor blueSeis-3A in a huddle test in Fürstfeldbruck. *Sensors*, *21*(3170), 1–20. <https://doi.org/10.3390/s21093170>
- Jousset, P., Currenti, G., Schwarz, B., Chalari, A., Tilmann, F., Reinsch, T., et al. (2022). Fibre optic distributed acoustic sensing of volcanic events. *Nature Communications*, *13*, 1753. <https://doi.org/10.1038/s41467-022-29184-w>
- Jousset, P., Budi-Santoso, A., Jolly, A. D., Boichu, M., Dwiyono, S., Sumarti, S., et al. (2013). Signs of magma ascent in LP and VLP seismic events and link to degassing: An example from the 2010 explosive eruption at Merapi volcano, Indonesia. *Journal of Volcanology and Geothermal Research*, *261*, 171–192. <https://doi.org/10.1016/j.jvolgeores.2013.03.014>
- Jurkevics, A. (1988). Polarization analysis of three-component array data. *Bulletin of the Seismological Society of America*, *78*(5), 1725–1743.
- Krueger, F., & Weber, M. (1992). The effect of low-velocity sediments on the mislocation vectors of the GRF array. *Geophysical Journal International*, *108*(1), 387–393. <https://doi.org/10.1111/j.1365-246X.1992.tb00866.x>
- Langston, C. A., & Liang, C. (2008). Gradiometry for polarized seismic waves. *Journal of Geophysical Research*, *113*(8), 1–15. <https://doi.org/10.1029/2007JB005486>
- Lindner, F., Wassermann, J., Schmidt-Aursch, M. C., Schreiber, K. U., & Igel, H. (2017). Seafloor ground rotation observations: Potential for improving signal-to-noise ratio on horizontal OBS components. *Seismological Research Letters*, *88*(1), 32–38. <https://doi.org/10.1785/0220160051>
- Lokmer, I., Bean, C. J., Saccorotti, G., & Patanè, D. (2007). Moment-tensor inversion of LP events recorded on Etna in 2004 using constraints obtained from wave simulation tests. *Geophysical Research Letters*, *34*(22), 1–6. <https://doi.org/10.1029/2007GL031902>
- Lokmer, I., Saccorotti, G., Di Lieto, B., & Bean, C. J. (2008). Temporal evolution of long-period seismicity at Etna Volcano, Italy, and its relationships with the 2004–2005 eruption. *Earth and Planetary Science Letters*, *266*(1–2), 205–220. <https://doi.org/10.1016/j.epsl.2007.11.017>
- Lomax, A., Michelini, A., & Curtis, A. (2009). Earthquake location, direct, global-search methods. In R. A. Meyers (Ed.), *Encyclopedia of complexity and systems science* (pp. 1–33). Springer. https://doi.org/10.1007/978-3-642-27737-5_150-2
- Maeda, Y., Takeo, M., & Ohminato, T. (2011). A waveform inversion including tilt: Method and simple tests. *Geophysical Journal International*, *184*(2), 907–918. <https://doi.org/10.1111/j.1365-246X.2010.04892.x>

- McNutt, S. R. (2005). Volcanic seismology. *Annual Review of Earth and Planetary Sciences*, 33(1), 461–491. <https://doi.org/10.1146/annurev.earth.33.092203.122459>
- Milana, G., Rovelli, A., De Sortis, A., Calderoni, G., Coco, G., Corrao, M., & Marsan, P. (2008). The role of long-period ground motions on magnitude and damage of volcanic earthquakes on Mt. Etna, Italy. *Bulletin of the Seismological Society of America*, 98(6), 2724–2738. <https://doi.org/10.1785/0120080072>
- Napoli, R., Currenti, G., & Sicali, A. (2021). Magnetic signatures of subsurface faults on the northern upper flank of Mt Etna (Italy). *Annals of Geophysics*, 64(1), PE108. <https://doi.org/10.4401/ag-8582>
- Neidell, N. S., & Taner, M. T. (1971). Semblance and other coherency measures for multichannel data. *Geophysics*, 36(3), 482–497. <https://doi.org/10.1190/1.1440186>
- Palaseanu-Lovejoy, M., Bisson, M., Spinetti, C., Buongiorno, M. F., Alexandrov, O., & Cerere, T. (2020). *Digital surface model of Mt. Etna Italy, derived from 2015 Pleiades Satellite Imagery*. U.S. Geological Survey Data Release. <https://doi.org/10.5066/P9IGLDYIE>
- Patane, D., Aliotta, M., Cannata, A., Cassisi, C., Coltelli, M., Di Grazia, G., et al. (2000). Interplay between Tectonics and Mount Etna's volcanism: Insights into the geometry of the plumbing system. In U. Schattner (Ed.), *New frontiers in tectonic research: At the midst of plate convergence* (p. 352). InTech. <https://doi.org/10.5772/23503>
- Patane, D., Di Grazia, G., Cannata, A., Montalto, P., & Boschi, E. (2008). Shallow magma pathway geometry at Mt. Etna volcano. *Geochemistry, Geophysics, Geosystems*, 9(12). <https://doi.org/10.1029/2008GC002131>
- Patane, D., Ferrucci, F., & Gresta, S. (1994). Spectral features of microearthquakes in volcanic areas: Attenuation in the crust and amplitude response of the site at Mt. Etna, Italy. *Bulletin of the Seismological Society of America*, 84(6), 1842–1860.
- Rodgers, P. W. (1968). The response of the horizontal pendulum seismometer to Rayleigh and Love waves, tilt, and free oscillations of the Earth. *Bulletin of the Seismological Society of America*, 58(5), 1385–1406. <https://doi.org/10.1785/BSSA0580051385>
- Rost, S., & Thomas, C. (2002). Array seismology: Methods and applications. *Reviews of Geophysics*, 40(3), 2-1–2-27. <https://doi.org/10.1029/2000RG000100>
- Saccorrotti, G., & Lokmer, I. (2021). Chapter 2 - A review of seismic methods for monitoring and understanding active volcanoes. In P. Papale (Ed.), *Forecasting and planning for volcanic hazards, risks, and disasters* (Vol. 2, pp. 25–73). Elsevier. <https://doi.org/10.1016/B978-0-12-818082-2.00002-0>
- Saccorrotti, G., Lokmer, I., Bean, C. J., Di Grazia, G., & Patanè, D. (2007). Analysis of sustained long-period activity at Etna Volcano, Italy. *Journal of Volcanology and Geothermal Research*, 160(3–4), 340–354. <https://doi.org/10.1016/j.jvolgeores.2006.10.008>
- Saccorrotti, G., Zuccarello, L., Del Pezzo, E., Ibanez, J., & Gresta, S. (2004). Quantitative analysis of the tremor wavefield at Etna Volcano, Italy. *Journal of Volcanology and Geothermal Research*, 136(3–4), 223–245. <https://doi.org/10.1016/j.jvolgeores.2004.04.003>
- Schweitzer, J. (2001). Slowness corrections - One way to improve IDC products. *Pure and Applied Geophysics*, 158(1), 375–396. <https://doi.org/10.1007/PL00001165>
- Sollberger, D., Greenhalgh, S. A., Schmelzbach, C., Van Renterghem, C., & Robertsson, J. O. A. (2018). 6-C polarization analysis using point measurements of translational and rotational ground-motion: Theory and applications. *Geophysical Journal International*, 213(1), 77–97. <https://doi.org/10.1093/gji/ggx542>
- Sollberger, D., Igel, H., Schmelzbach, C., Edme, P., van Manen, D. J., Bernauer, F., et al. (2020). Seismological processing of six degree-of-freedom ground-motion data. *Sensors*, 20(23), 1–32. <https://doi.org/10.3390/s20236904>
- Soubestre, J., Shapiro, N. M., Seydoux, L., de Rosny, J., Droznin, D. V., Droznina, S. Y., et al. (2018). Network-based detection and classification of seismovolcanic tremors: Example from the Klyuchevskoy volcanic group in Kamchatka. *Journal of Geophysical Research: Solid Earth*, 123(1), 564–582. <https://doi.org/10.1002/2017JB014726>
- Taisne, B., Brenguier, F., Shapiro, N. M., & Ferrazzini, V. (2011). Imaging the dynamics of magma propagation using radiated seismic intensity. *Geophysical Research Letters*, 38(4). <https://doi.org/10.1029/2010GL046068>
- Trnkoczy, A. (2012). Understanding and parameter setting of STA/LTA trigger algorithm. In *New manual of seismological observatory practice (NMSOP)* (Vol. 2, pp. 1–41). Deutsches GeoForschungsZentrum GFZ. https://doi.org/10.2312/GFZ.NMSOP-2_IS_8.11
- Van Driel, M., Wassermann, J., Pelties, C., Schiemenz, A., & Igel, H. (2015). Tilt effects on moment tensor inversion in the near field of active volcanoes. *Geophysical Journal International*, 202(3), 1711–1721. <https://doi.org/10.1093/gji/ggv209>
- Wassermann, J. (2012). *Volcano seismology* (Technical Report). Deutsches GeoForschungsZentrum GFZ. https://doi.org/10.2312/GFZ.NMSOP-2_ch13
- Wassermann, J., Bernauer, F., Shiro, B., Johanson, I., Guattari, F., & Igel, H. (2020). Six-axis ground motion measurements of caldera collapse at Kilauea volcano, Hawai'i—More data, more puzzles? *Geophysical Research Letters*, 47(5), 1–7. <https://doi.org/10.1029/2019GL085999>
- Wassermann, J., Braun, T., Ripepe, M., Bernauer, F., Guattari, F., & Igel, H. (2021). The use of 6DOF measurement in volcano seismology – An application to Stromboli volcano. *Journal of Volcanology and Geothermal Research*, 424, 107499. <https://doi.org/10.1016/j.jvolgeores.2022.107499>
- Wassermann, J., Wietek, A., Hadziioannou, C., & Igel, H. (2016). Toward a single-station approach for microzonation: Using vertical rotation rate to estimate love-wave dispersion curves and direction finding. *Bulletin of the Seismological Society of America*, 106(3), 1316–1330. <https://doi.org/10.1785/0120150250>
- Wielandt, E., & Forbriger, T. (1999). Near-field seismic displacement and tilt associated with the explosive activity of Stromboli. *Annali di Geofisica*, 42(3). <https://doi.org/10.4401/ag-3723>
- Yuan, S., Simonelli, A., Lin, C. J., Bernauer, F., Donner, S., Braun, T., et al. (2020). Six degree-of-freedom broadband ground-motion observations with portable sensors: Validation, local earthquakes, and signal processing. *Bulletin of the Seismological Society of America*, 110(3), 953–969. <https://doi.org/10.1785/0120190277>
- Zieger, T., Sens-Schönfelder, C., Ritter, J. R., Lühr, B. G., & Dahm, T. (2016). P-wave scattering and the distribution of heterogeneity around Etna volcano. *Annals of Geophysics*, 59(4). <https://doi.org/10.4401/ag-7085>
- Zuccarello, L., Burton, M. R., Saccorrotti, G., Bean, C. J., & Patanè, D. (2013). The coupling between very long period seismic events, volcanic tremor, and degassing rates at Mount Etna volcano. *Journal of Geophysical Research: Solid Earth*, 118(9), 4910–4921. <https://doi.org/10.1002/jgrb.50363>
- Zuccarello, L., Paratore, M., La Rocca, M., Ferrari, F., Messina, A., Branca, S., et al. (2016). Shallow velocity model in the area of Pozzo Pitarone, Mt. Etna, from single station, array methods and borehole data. *Annals of Geophysics*, 59(4). <https://doi.org/10.4401/ag-7086>